日本磁気学会
ISSN 2432-0250
Journal of the Magnetics Society of Japan
Electronic Journal URL: https://www.jstage.jst.go.jp/browse/msjmag

Vol.42 No.5　2018

Journal

Magnetic Recording

JOURNAL OF THE MAGNETICS SOCIETY OF JAPAN

Vol.42 No.5 2018

日本磁気学会

ISSN 2432-0250

HP: http://www.magnetics.jp/ e-mail: msj@bj.wakwak.com

Electronic Journal: http://www.jstage.jst.go.jp/browse/msjmag

世界初！
高温超電導型VSM

新製品

世界初*、高温超電導マグネットをVSMに採用することで
測定速度 当社従来機1/20を実現。
0.5mm cube磁石のBr, HcJ高精度測定が可能と
なりました。
*2014年7月 東英工業調べ

測定結果例

高温超電導VSMによるNdFeB(sint.) 0.5mm cube BHカーブ

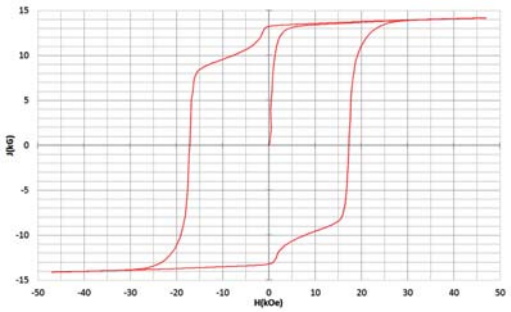

磁化測定レンジ：0.2emu
Br = 13.2kG　　HcJ = 17.2kOe

高温超電導VSMによるNdFeB(sint.) 1mm cube BHカーブ

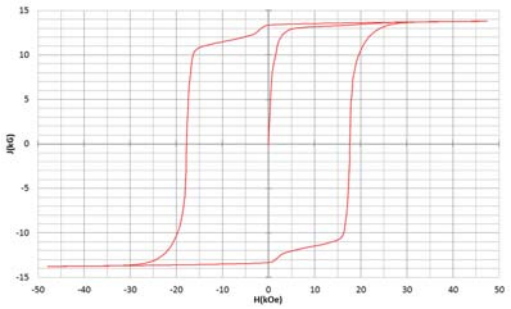

磁化測定レンジ：2emu
Br = 13.3kG　　HcJ = 17.7kOe

高温超電導VSMによるNdFeB(sint.) 4mm cube BHカーブ

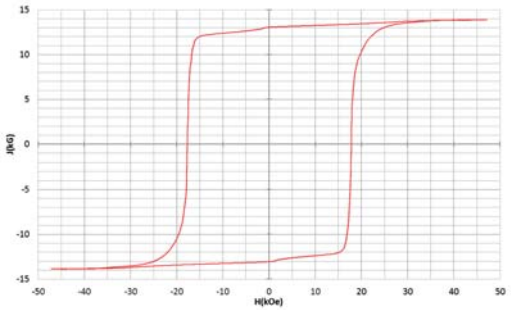

磁化測定レンジ：100emu
Br = 13.1kG　　HcJ = 17.8kOe

高速測定を実現

高温超電導マグネット採用により、高速測定を実現しました。Hmax= 5Tesla, Full Loop 測定が2分で可能です。
（当社従来機：Full Loop測定　40分）

小試料のBr,HcJ高精度測定

0.5mm cube 磁石のBr,HcJ高精度測定ができ、表面改質領域を切り出しBr,HcJの強度分布等、微小変化量の比較測定が可能です。
また、試料の加工劣化の比較測定が可能です。

試料温度可変測定

−50℃～+200℃温度可変UNIT（オプション）

磁界発生部の小型化

マグネットシステム部寸法：0.8m×0.3m×0.3m

TOEI 東英工業株式会社
http://www.toeikogyo.co.jp
〒194-0035 東京都町田市忠生1-8-13
TEL：042-791-1211 FAX：042-792-0490
E-mail : sales@toeikogyo.co.jp

有限要素法解析ソフトウェア COMSOL Multiphysics®

COMSOL MULTIPHYSICS®

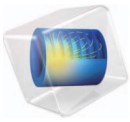

マルチフィジックスの進化論

無制限・強連成で実現象に即したシミュレーション事例のご紹介

COMSOLご紹介セミナー

COMSOL Multiphysics®で、電磁界に加えて、構造・機械・振動・流体・伝熱、さらに加えて化学反応工学まで連成できるシミュレーションを始めませんか？

東京(神田)会場:10月24日、2019年1月23日

13:30開始～16:30終了 (当日、個別のご相談も承ります)

※埼玉県さいたま市と福島での開催を計画中です

参加費用：**無料** (事前申し込み制)

詳細とお申し込みはコチラ：

http://www.kesco.co.jp/comsol_intro.html

皆様の拠点にお伺いしてオンサイト開催も承ります

永久磁石を利用した磁気軸受の解析例

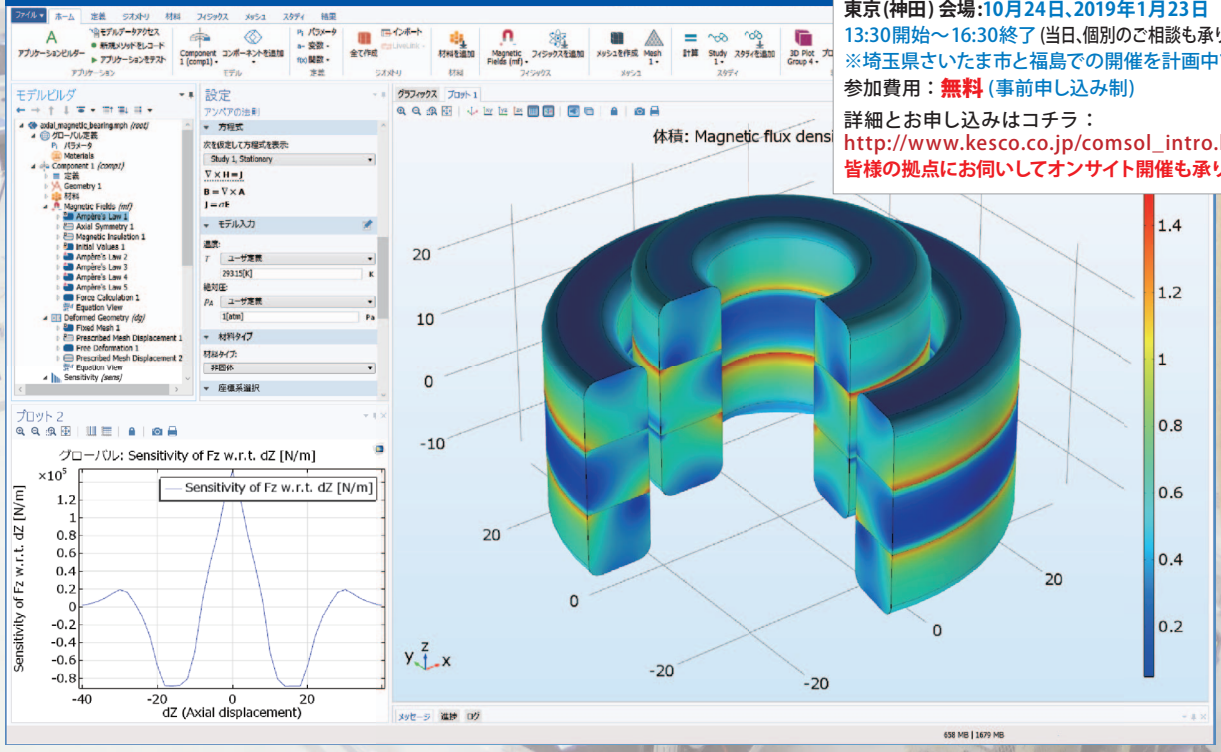

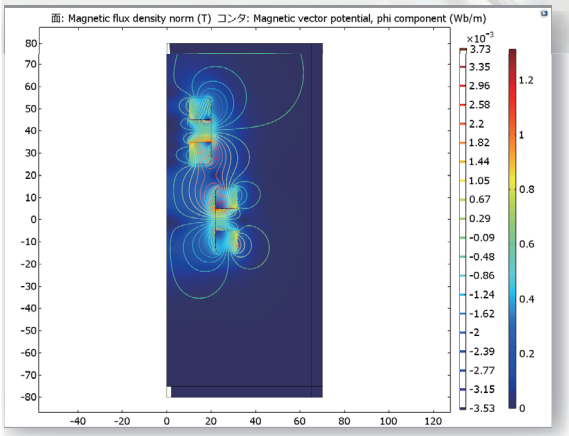

AC/DC モジュールの適用例

- AC/DC 電流分布、電場分布
- バイオヒーティング
- コイルとソレノイド
- SPICE 回路とフィールドシミュレーション
- 接触抵抗
- 電磁両立性 (EMC) および電磁妨害 (EMI)
- 電磁力およびトルク
- 電磁力シールド
- 電気機械の変形
- ホール効果を利用したセンサ
- インシュレータ、コンデンサ、誘電体
- モータ、ジェネレータ、および他の電気機械
- 非線形材料
- 寄生容量とインダクタンス
- 永久磁石と電磁石
- 多孔質材料
- 抵抗および誘導加熱
- センサ
- 超伝導体
- 変圧器とインダクタ

永久磁石を使用した磁気軸受

永久磁石を使用した軸受はターボ機械、ポンプ、モータ、発電機やフライホイール式エネルギー貯蔵システムなど、様々な分野で使用されています。非接触かつ潤滑不要で保守整備を大幅に省略できる点は、従来の機械式ベアリングと比べて重要なメリットです。この例では、軸方向の永久磁石軸受の磁気力と剛性などの設計パラメータを計算する方法を示しています。

※AC/DCモジュールはCOMSOL Multiphysicsと併用するアドオン製品です。

COMSOL Multiphysics® なら、今まで不可能だった３種以上のマルチフィジックス解析を強連成で実現できます。30日間全機能無料トライアル、無料の導入セミナー、1000種を超える世界の様々な事例をご提供いたします。詳しくは、下記の弊社営業部までお問い合せください。

COMSOL

http://www.comsol.jp

COMSOL CONFERENCE
2018 TOKYO
Friday, December 7th, 2018 : Akihabara, Tokyo, JAPAN
http://www.kesco.co.jp/conference/

KESCO KEISOKU ENGINEERING SYSTEM
計測エンジニアリングシステム株式会社
http://www.kesco.co.jp/comsol/
Tel : 03-5282-7040 ・ Fax : 03-5282-0808

Journal of the Magnetics Society of Japan
Vol. 42, No. 5

Electronic Journal URL: https://www.jstage.jst.go.jp/browse/msjmag

CONTENTS

J. Magn. Soc. Jpn., **42**, 102-109 (2018)

<Paper>

Growth of $L1_0$-ordered Crystal in FePt Epitaxial Magnetic Thin Films on (001) Oriented Substrates

Masaaki Futamoto, Tomoki Shimizu, Masahiro Nakamura, and Mitsuru Ohtake
Faculty of Science and Engineering, Chuo University, *1-13-27 Kasuga, Bunkyo-ku, Tokyo 112-8551, Japan*

Effects of MgO cap-layer and substrate on $L1_0$-ordered FePt film structure are investigated by high-resolution transmission electron microscopy (TEM) for FePt thin films prepared on (001) oriented substrates by using a two-step method consisting of low temperature (200 °C) film formation followed by high temperature (600 °C) annealing. The TEM observation has shown that the crystal lattice of $A1$-FePt film (10 nm thickness) on MgO(001) substrate with 2-nm-thick MgO cap-layer is strained in the lateral direction to substrate surface, and by annealing the film structure varies to $L1_0$-ordered phase consisting of $L1_0$(001) variant with the c-axis aligned perpendicular. The FePt film in a sample of $L1_0$-FePt(2 nm)/VN(001) is consisting of $L1_0$-(001) variant, whereas the FePt film in a $L1_0$-FePt(2-nm average thickness)/MgO(001) sample includes variants of $L1_0$(100),(010) with the c-axis lying in-plane in addition to $L1_0$(001) variant. The lattice mismatch with substrate material is decreased by introduction of misfit dislocation and by lattice bending in $L1_0$-FePt crystal. The variant structures are interpreted to be influenced by the lattice strain in $A1$-FePt film during the $L1_0$-crystal nucleation stage at the high temperature annealing process. Based on the experimental results, a model to explain the phase transformation from disordered $A1$ to ordered $L1_0$ involving nucleation and growth of $L1_0$-crystal is proposed.

Key words: $L1_0$-ordered phase, $A1$-disordered phase, FePt thin film, variant structure, c-axis, surface roughness

1. Introduction

FePt alloy thin films with $L1_0$-ordered structure have been investigated for magnetic recording media and MRAM applications. For such device applications, the easy magnetization axis, c-axis of $L1_0$-ordered structure, must be controlled to be perpendicular while achieving a high ordering degree and a very smooth flat surface. Various substrate/underlayer materials such as CrRu [1], Pt [2], Ta [3], MgO [4], $SrTiO_3$, $LaAlO_3$, $KTaO_3$ [5], AlN [6], etc. have been investigated to align the crystal orientation. Epitaxial thin film growth on (001) oriented substrate/underlayer with the lattice constant slightly larger than that of $L1_0$-FePt crystal has been shown effective for aligning the c-axis perpendicular where an in-plane lattice strain in FePt material caused by the mismatch with substrate is providing a favorable condition for $L1_0$-crystal nucleation with the c-axis perpendicular to the substrate surface.[7,8] For promotion of $L1_0$-ordering, process temperatures higher than 500 °C are required, which generally enhance film surface undulations through by faceting and by de-wetting of FePt material on the substrate.[9-11] Two-step process consisting of low temperature film deposition followed by high temperature annealing has been tried for improving the crystallographic quality, the c-axis orientation, and the magnetic properties of $L1_0$-ordered FePt thin film.[12,13] The authors have confirmed that the two-step process is effective for not only the preparation of c-axis perpendicularly oriented thin films with good crystallographic quality but also for the preparation of $L1_0$-ordered films with very flat surfaces.[14,15] However, when the film thickness was decreased to be less than several nanometers, which would be the thickness range of $L1_0$-ordered FePt film for future device applications, de-wetting of FePt material took place on MgO substrate and the film morphology became discontinuous consisting of $L1_0$-ordered crystal islands.[7,15] The volume fraction of c-axis in-plane oriented $L1_0$-crystal increased when de-wetting took place. In order to suppress de-wetting, an employment of underlayer material with the surface energy larger than that of MgO was considered effective in reducing the contact angle between an isolated FePt island-like crystal and the substrate. The authors have shown that VC and VN materials with lattice constants similar to that of MgO but with higher surface energies are useful for underlayers to prepare continuous $L1_0$-ordered thin films with flat surfaces.[16] For preparation of thin film with flat surface, formation of cap-layer consisting of material like FeO_x [17] and SiO_2 [18] has been applied on top of magnetic thin film during the film deposition process. In particular, MgO cap-layer formation on top of FePt thin film at low temperature deposition process has been confirmed effective for the preparation of $L1_0$-ordered thin film with enhanced degree of ordering.[19-21] The volume fraction of c-axis in-plane oriented $L1_0$-crystal also decreased and the perpendicular magnetic property has been improved remarkably. The cap-layer was interpreted to be providing lateral strain to the FePt magnetic thin film from top side thus enhancing formation of $L1_0$ (001) crystal. Although lateral stress in FePt thin film and surface energy difference between FePt and substrate materials are interpreted to be giving strong influence on the formation of (001)-oriented FePt films, detailed atomic structure variation around material interfaces, cap-layer/FePt and FePt/substrate, have not yet been made clear in relation to the phase transformation from disordered $A1$-phase to ordered $L1_0$-phase.

In the present study, film growth structures are investigated by employing a high-resolution transmission electron microscope (TEM) for epitaxial thin films prepared by employing the two-step method, both for disordered $A1$-FePt(001) and ordered $L1_0$-FePt(001) films with MgO cap-layers. The detailed interface structures are also investigated for $L1_0$-ordered FePt ultra-thin films of 2 nm in average thickness without cap-layer formed on epitaxial underlayers of MgO(001) and VN(001). The morphology and the epitaxial growth structure of $A1$- and $L1_0$-FePt crystals are studied in atomic detail for the

Table 1 Samples for TEM observation and related material parameters.

Sample structure	Temperature	FePt structure	Order degree [a)]	vol. %, $L1_0(001)$ [b)]	R_a [c)]
MgO(2 nm)/FePt(10 nm)/MgO(001)	200 °C	Disordered $A1$	-	-	0.1 nm
MgO(2 nm)/FePt(10 nm)/MgO(001)	200 °C→600°C	Ordered $L1_0$	0.8	100	0.1 nm
FePt(2 nm)/MgO(001)(2 nm)/$SrTiO_3$(001)	200 °C→600°C	Ordered $L1_0$	0.1	80	4.2 nm
FePt(2 nm)/VN(001)(2 nm)/$SrTiO_3$(001)	200 °C→600°C	Ordered $L1_0$	0.2	100	0.1 nm

Parameters of material used in the present study

Material	Crystal structure	Melting point	Young's modulus	Surface energy [g)]
$A1$-FePt	Cubic, a = 0.3830 nm	1500 °C	194 – 158 GPa [d)]	2.1 J/m^2
$L1_0$-FePt	a = 0.3842 nm ,c = 0.3702 nm, c/a = 0.96	(Ordered phase <1300 °C)		
MgO	Cubic (NaCl-type), a = 0.4212 nm	2800 °C	345 GPa [e)]	1.5 J/m^2
VN	Cubic (NaCl-type), a = 0.4136 nm	2050 °C	421 GPa [f)]	2.7 J/m^2
$SrTiO_3$	Cubic (Perovskite), a = 0.3905 nm	2080 °C	-	-

a, b) $L1_0$-ordering degree and volume percent of $L1_0(001)$ variant were determined by using XRDs. The details are reported in Refs. 15,16,20.
c) Surface roughness, R_a, was measured by AFM.
d) Y. J. Chiu, C. Y. Shen, S. R. Jian, H. W. Chang, J. Y. Juang, Y. Y. Liao, and C. L. Fan, *Nanosci. Nnaotechnol. Lett.*, 8, 260, 2016.
e) G. V. Samsonov (ed.), in *Physical and chemical properties of oxides* (Metallurgy, Moscow, 1973).
f) G. V. Samsonov and I. M. Vnytky (ed.), in *Handbook of refractory compounds* (Metallurgy, Moscow, 1976).
g) The values are cited from Ref. 16.

cross-sectional samples, and the technology for preparing a very thin $L1_0$-FePt film with the easy magnetization axis controlled to be perpendicular to the substrate surface is discussed from a view point of nucleation and growth of $L1_0$-ordered phase.

2. Experimental Procedure

2.1 Film preparation

Thin films were prepared on (001) single-crystal base substrates of MgO and $SrTiO_3$ by using a radio-frequency (RF) magnetron sputtering system equipped with a RHEED facility. The base pressures were lower than 4 x 10^{-7} Pa. Substrates were heated at 600 °C for 1 hour to clean surfaces. $Fe_{50}Pt_{50}$ (at.%), MgO, and VN targets of 3-inch-diameter were employed and the RF powers were set at 43, 200, and 96 W where the deposition rates of FePt, MgO, and VN were 0.020, 0.015, and 0.020 nm/s, respectively. Two sets of sample were prepared for structure analysis. One is with a film thickness of 10 nm formed on MgO(001) substrate and with MgO cap-layer, and the other is with a thickness of 2 nm formed on (001) oriented MgO and VN underlayers with no cap-layers.

In the first case, FePt and MgO materials were deposited sequentially in 10 and 2 nm respective thicknesses at 200 °C on MgO(001) substrate, and then annealed at 600 °C for 1 hour. RHEED observation confirmed that films formed at 200 °C were grown epitaxially on the MgO substrate in a crystallographic relationship of $MgO(001)[100]_{cap\text{-}layer}$ // $A1$-FePt(001)[100] // $MgO(001)[100]_{substrate}$. After annealing at 600 °C, the relationship varied to $MgO(001)[100]_{cap\text{-}layer}$ // $L1_0$-FePt(001)[100] // $MgO(001)[100]_{substrate}$. For the second set of samples, 2-nm-thick underlayers of MgO and VN were formed on $SrTiO_3$(001) substrates at 600 °C and then FePt material was deposited at 200 °C on the underlayers in 2-nm average thickness. Here, a base substrate of $SrTiO_3$(001) was employed for simple preparation of (001) oriented MgO and VN underlayers by hetero-epitaxy where the lattice mismatches are -7.3 and -5.6 % for the underlayer materials, respectively. Then the samples were annealed at 600 °C for 1 hour for $L1_0$-ordering. The crystallographic orientation relationships of $L1_0$-FePt(001),(100),[100]// $MgO(001)[100]_{underlayer}$, $VN(001)[100]_{underlayer}$ // $SrTiO_3(001)[100]_{substrate}$ were determined by RHEED and XRD.

2.2 Structure observation

Table 1 lists the samples for TEM observation and the related material parameters. The $L1_0$-ordering degree and the volume fraction of $L1_0$-crystal variants were determined by XRD, and the surface roughness, R_a, was measured by AFM as reported in our previous papers.[8,15,16,19] The magnetic properties of these samples are also reported in the references.[16,20] Cross-sectional samples were prepared by employing a focused ion-beam sampling technique. TEM observation was carried out by using a Hitachi STEM (HD-2700) equipped with an EDX facility (AMETEK EDAX Octane T Ultra W) for elemental analysis at an acceleration voltage of 200 kV.

3. Results and Discussion

3.1 FePt film with disordered $A1$ structure

Figure 1 shows the cross-sectional TEM image of MgO/$A1$-FePt/MgO sample and the diffraction patterns corresponding to the MgO cap-layer, the $A1$-FePt film, and the MgO substrate which are obtained through first

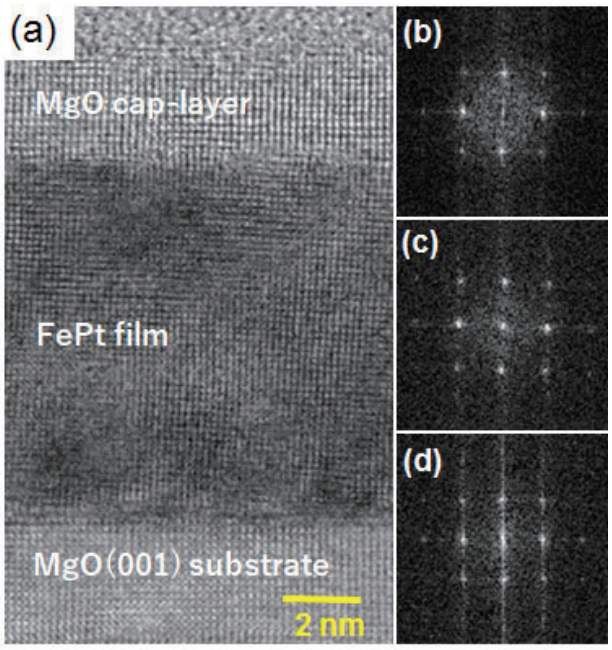

Fig. 1 Cross-sectional TEM image of MgO/*A*1-FePt/MgO sample (a), and diffraction patterns corresponding to (b) MgO cap-layer, (c) *A*1-FePt film, and (d) MgO substrate. The diffraction patterns are obtained through FFT of the respective bright-field TEM image areas shown in (a).

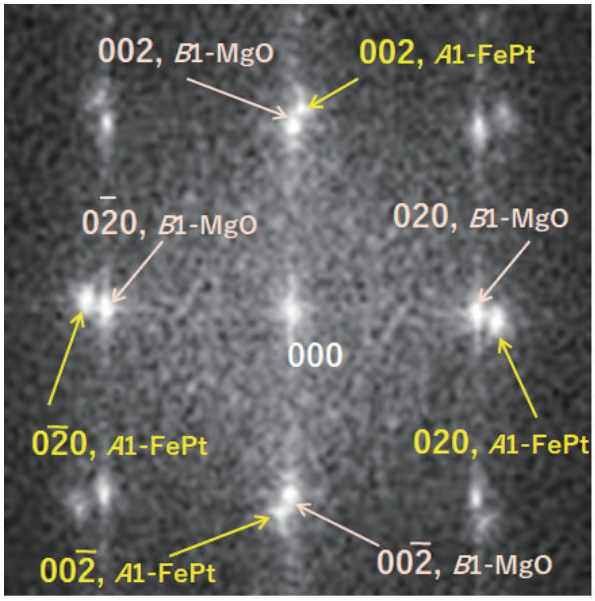

Fig. 2 Diffraction pattern obtained from the whole sample area shown in the bright-field TEM image of Fig. 1 (a). The diffraction spots are indexed based on *A*1-FePt and *B*1-MgO crystal structures.

Fourier transformation (FFT) of the respective bright-field TEM image areas shown in Fig. 1(a). The diffraction patterns, (b)-(d), indicate that the MgO cap-layer and the FePt film are (001) oriented single crystals and they are epitaxially grown on the MgO(001) substrate in the crystallographic orientation relationship determined by RHEED. The continuous lattice images crossing the FePt/MgO and the

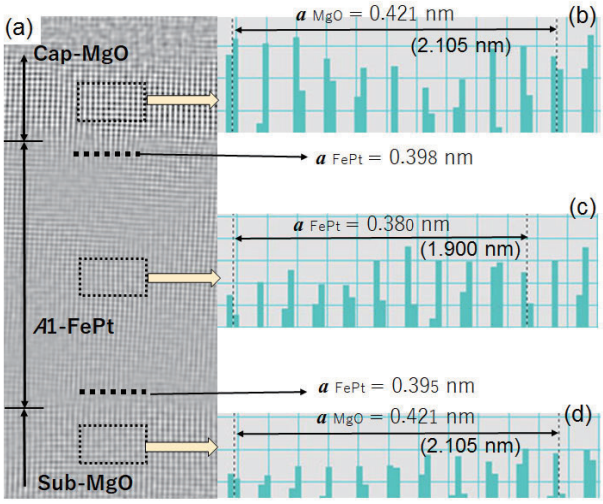

Fig. 3 Inverse-FFT filtered TEM image of MgO/*A*1-FePt/MgO sample (a). In-plane lattice distances are measured using a software equipped with the TEM and local in-plane lattice parameters are estimated (b)-(d).

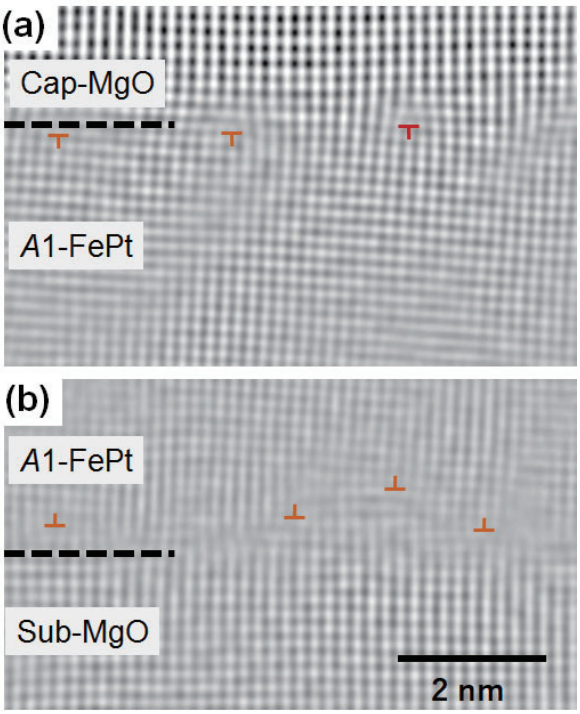

Fig. 4 Inverse-FFT images of interfaces, (a) MgO cap-layer/*A*1-FePt and (b) *A*1-FePt/MgO substrate.

MgO/FePt interfaces shown in Fig. 1(a), are clearly showing the epitaxial growth of these materials on the base substrate of MgO(001). The thickness of MgO cap-layer in the TEM image is slightly larger than the nominal thickness of 2 nm, which is attributed to an experimental error during the sputter deposition process. The diffraction pattern from FePt film indicates that the structure is *A*1 (fcc) with disordered atomic arrangement. Figure 2 shows the diffraction pattern obtained by FFT from whole sample area including MgO cap-layer, *A*1-FePt film, and MgO

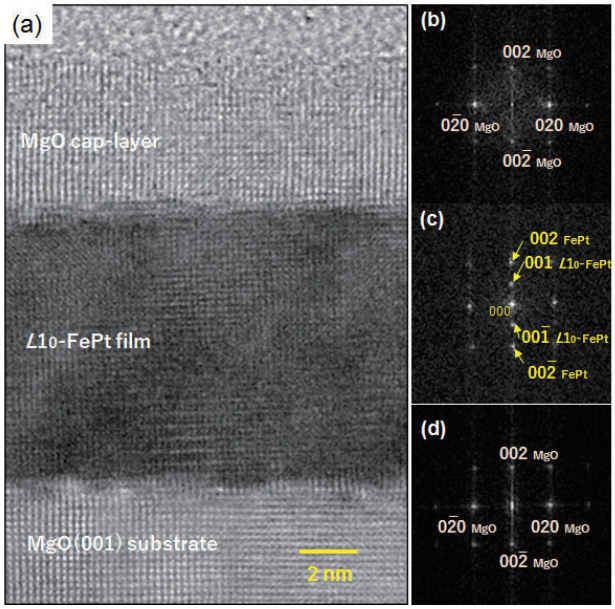

Fig. 5 Cross-sectional TEM image of MgO-cap-layer/FePt(10 nm)/MgO(001) sample after annealing at 600 °C, (a), and the diffraction patterns obtained by FFT of the bright-field TEM image areas of (b) cap-layer, (c) FePt film, and (d) MgO substrate, respectively.

substrate. The patterns are indexed based on *A*1-FePt and *B*1-MgO crystal structures. Broader diffraction patterns from *A*1-FePt layer, 020 and 0-20 reflections, in comparison to those from *B*1-MgO are suggesting that the lattice parameter, $a_{FePt,}$ measured in in-plane direction of *A*1-FePt crystal involves variations depending on the sample local area. To accurately measure the lattice variation, the TEM image is filtered by using an inverse-FFT technique employing {020} reflections from *A*1-FePt and *B*1-MgO crystals. Figure 3(a) shows the inverse-FFT filtered TEM image where the {020} lattice images of *A*1-FePt and *B*1-MgO crystals are more clearly visualized than in the bright-field TEM image. The values of (020) lattice spacing are measured for the regions circled by dotted squares as shown in Figs. 3(b), (c), and (d), respectively. The in-plane lattice distance of MgO, a_{MgO}, is same for the substrate and the cap-layer, which shows the rigid nature of this material. By assuming the a_{MgO} to be same with the bulk lattice constant (0.4212 nm) as a reference, it is possible to estimate the variation of a_{FePt} along the film growth direction. From local lattice images, the in-plane lattice parameter, a_{FePt}. is measured to be 0.380 nm for the central region while those near the substrate and the cap-layer are measured to be 0.395 and 0.398 nm, respectively as indicated in Fig. 3. The lattice flexibility of FePt is apparently reflecting the mechanical property, Young's modulus, of the material. As shown in Table 1, MgO has a higher Young's modulus (345 GPa) than that of FePt (194-158 GPa). For the 10-nm-thick *A*1-FePt epitaxial thin film, a_{FePt} is expanded and approaching to the value of a_{MgO} in regions close to the substrate and also to the cap-layer, whereas the a_{FePt} value in the central part is measured to be nearly similar to the lattice constant of bulk *A*1-crystal (a = 0.3830 nm). The MgO(001) crystal is giving lateral strain to the *A*1-FePt from both the substrate and the cap-layer sides. The result is in agreement with the study on *A*1-FePt(001) epitaxial thin films investigated by XRDs where a_{FePt} is reported to approach to that of a_{MgO} when *A*1-FePt film thickness is decreased.[7)]

Figure 4 shows the inverse-FFT images of interfaces, (a) MgO cap-layer/ *A*1-FePt and (b) *A*1-FePt/MgO substrate. The (020) lattice-line images of *A*1-FePt are slightly bending and misfit dislocations are recognized within the *A*1-FePt film, whereas the (020) lattice-line images of MgO are observed to be nearly straight reflecting the rigid mechanical property of this material. The lattice strain caused by the mismatch between the two materials (about 9 %) is mostly adjusted by deformation of *A*1-FePt(001) epitaxial thin film including introduction of misfit dislocations. The results indicate that an in-planes stress is caused in the *A*1-FePt(001) epitaxial thin film, which is expected to give an influence on the nucleation of $L1_0$-crystal when the material is heated at higher temperatures. The nucleation and growth mechanism will be discussed in a later section.

3.2 $L1_0$-ordered FePt film structure

Figure 5 shows the TEM image of MgO-cap-layer/FePt(10 nm)/MgO(001) sample after annealing at 600 °C and the diffraction patterns obtained by FFT of the bright-field TEM image areas of cap-layer, FePt film, and MgO substrate, respectively. Super lattice reflections from $L1_0$-ordered crystal, 001 and 00-1, are clearly observed while those from 010 and 0-10 are missing in Fig. 5(c). This indicates that the 10-nm-thick FePt film consists of $L1_0$(001) variant crystal with the *c*-axis perpendicular to the substrate surface, which is in agreement with the previous investigation carried out by XRDs.[15)] The (020) lattice line images are continuous from the substrate up to the cap-layer corresponding to the epitaxial relationship of $MgO(001)[100]_{cap\text{-}layer}$ // $L1_0$-$FePt(001)[100]$ // $MgO(001)[100]_{substrate}$. The result confirms that it is possible to align the *c*-axis of $L1_0$-crystal to be perpendicular to the substrate even for 10-nm-thick FePt film by applying an MgO cap-layer. It is known that 10-nm-thick FePt films formed on MgO(001) substrates without cap-layers include nearly 20 vol.% of $L1_0$-(100), (010) variant crystals with the *c*-axis lying in-plane when prepared under similar process conditions. [7, 20)]

Figure 6 shows the high-resolution TEM images around the cap-layer/FePt and the FePt/substrate interfaces. The lattices are continuous crossing the interfaces and misfit dislocations are observed only in the $L1_0$-FePt(001) crystal. Misfit dislocations are observed periodically, about every 10 lattice lines of MgO(020), in agreement with the previous reports [22,23)], and these dislocations are effectively decreasing the lattice misfit of 9 % to be nearly zero percent. A presence of crystallographic defect, A-B in Fig. 6(a), is also decreasing the lattice mismatch between the two materials, where no misfit dislocations are observed below the A-B defect. Such defect is considered to be formed by chance during the cap-layer formation process at the substrate temperature of 200 °C. High-resolution TEM image analysis, together with the

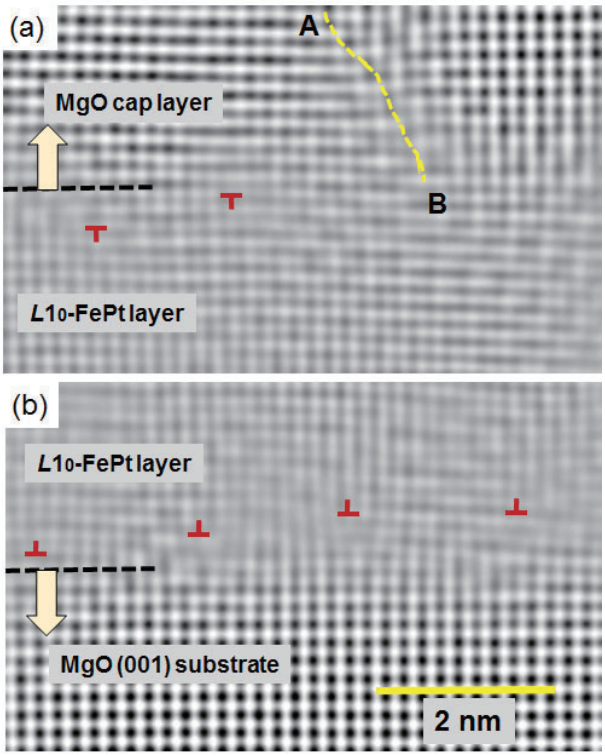

Fig. 6 High-resolution cross-sectional TEM images observed for (a) cap-layer/FePt and (b) FePt/substrate interfaces.

sharp diffraction from $L1_0$-ordered phase shown in Fig. 5 (c), indicate that the lattice strain in the $A1$-FePt film has been relieved during the 600 °C heating stage where nucleation and growth of $L1_0$-crystal proceeded through dynamic movement of Fe and Pt atoms within the epitaxial $A1$-FePt(001) film.

3.3 Structure of 2-nm-thick FePt film on (001) epitaxial underlayers

When an FePt thin film formed at low temperature (200 °C) is annealed at a higher temperature of 600 °C, atomic migration takes place within the film. Atomic migration is necessary in transforming the crystal structure from disordered $A1$ to an ordered phase of $L1_0$, but it also changes the film surface morphology. Film morphology variation tends to be enhanced for a thinner film, particularly for the thickness less than 10 nm. De-wetting of FePt material from a substrate or an underlayer leads to formation of a discontinuous film that consists of isolated crystalline islands. The authors have shown that it is possible to suppress such de-wetting by using an underlayer material with the surface energy higher than that of FePt material, such as VN and VC. [16, 21]

Figure 7 compares the cross-sectional TEM images observed for 2-nm-thick FePt films formed on MgO(001) and VN(001) underlayers grown epitaxially on base substrate of $SrTiO_3$(001). These samples were prepared by using the two-step method under similar process conditions. The structures of FePt films were confirmed by RHEED and XRD to be with $L1_0$-ordered structure. The FePt film formed on MgO underlayer has been shown by XRD analysis to include 20 vol. % of $L1_0$-(100), (010) variants with the c-axis lying in-plane. The film is

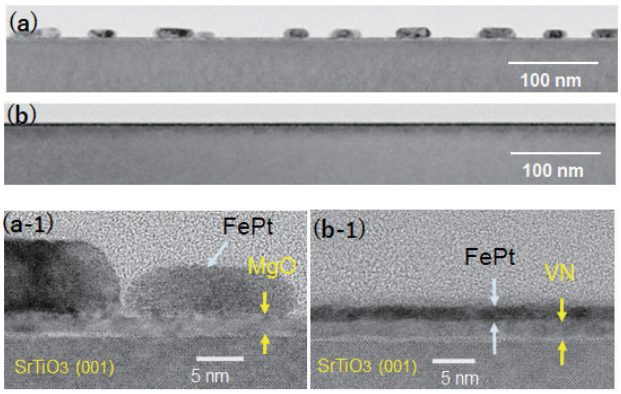

Fig. 7 Cross-sectional TEM images of FePt films with 2-nm average thickness formed on MgO(001) and VN(001) underlayers grown epitaxially on base substrate of $SrTiO_3$(001). (a), (a-1) FePt/MgO/$SrTiO_3$(001) sample, (b), (b-1) FePt/VN/$SrTiO_3$(001) sample.

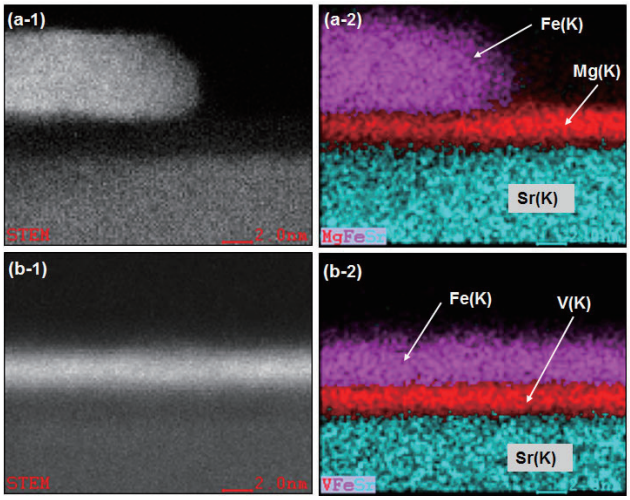

Fig. 8 Distributions of elements of samples, FePt(average thickness: 2 nm)/MgO(2 nm)/$SrTiO_3$(001) and FePt(2 nm)/VN(2 nm)/$SrTiO_3$(001), visualized by EDX imaging. (a-1), (b-1) dark-field TEM images and (a-2), (b-2) elemental distributions of respective sample.

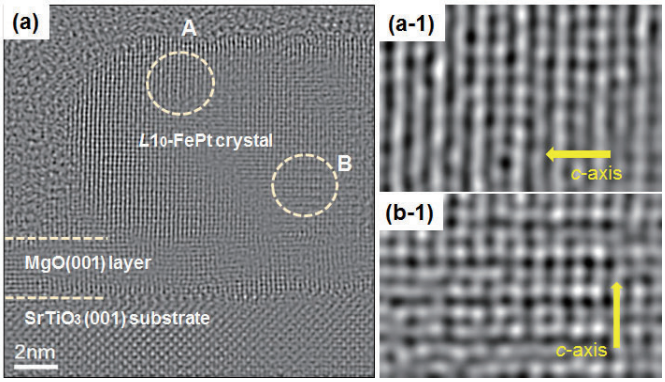

Fig. 9 Inverse-FFT TEM image of FePt/MgO/$SrTiO_3$(001) sample (a), and high magnification images of (a-1) region A and of (b-1) region B shown by dotted circles in (a).

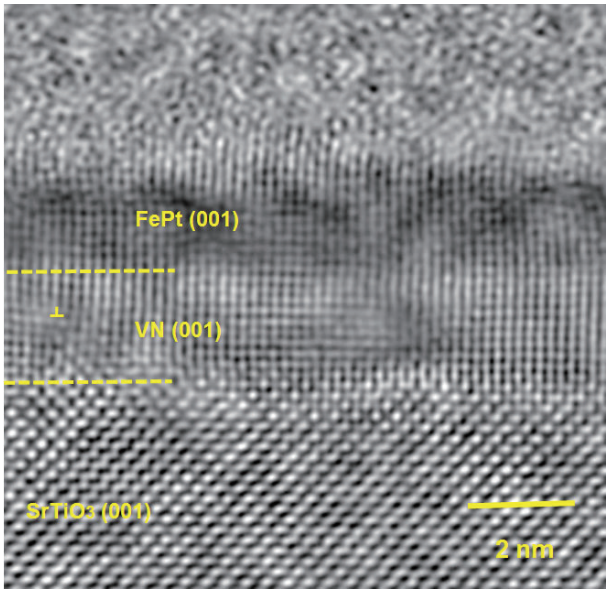

Fig. 10 Inverse-FFT high-resolution TEM image of FePt/VN/$SrTiO_3$(001) sample.

discontinuous and is consisting of isolated islands with the local thickness exceeding 10 nm. On the contrary, the film formed on VN underlayer is continuous and the surface undulations are less than 0.5 nm. Figure 8 shows the distributions of elements for the two samples, FePt(average thickness: 2 nm)/MgO(2 nm)/$SrTiO_3$(001) and FePt(2 nm)/VN(2 nm)/$SrTiO_3$(001), visualized by the EDX facility equipped with the TEM. The sharp elemental interfaces observed for these samples indicate that atomic diffusion crossing the interfaces is negligible.

Figure 9 shows the inverse-FFT high resolution TEM image of FePt/MgO/$SrTiO_3$(001) sample, where {200} reflections from FePt and MgO and {011} reflections from $SrTiO_3$(001) are employed for the image filtering. A large $L1_0$-FePt crystal with height of 9.4 nm is formed epitaxially on the 2-nm-thick MgO(001) underlayer. Although the (020) and (002) lattice images are continuous within the crystal, the lattice contrast looks different depending on the local region, for example between the areas of A and B shown as the dotted circles in Fig. 9(a). The distance between the two regions is less than 10 nm. In the A region, bright and dark lattice contrasts are observed in lateral direction, while those in the B region are observed in vertical direction. Considering that the lattice line contrast in TEM image depends on the atomic number, atomic stacking of Fe/Pt/Fe/Pt/---- is possibly realized in lateral direction in the A region which indicate that the *c*-axis is aligned in in-plane. The *c*-axis is presumably along the perpendicular direction in the region B. The FePt island is thus interpreted to be including $L1_0$-FePt(001) and $L1_0$-FePt(010) variants. The TEM image also suggests that nucleation of $L1_0$-crystal has taken place within the FePt island in different regions of A and B which are separated by a small distance of less than 10 nm. The result that $L1_0$-FePt(010) variant with the *c*-axis lying in in-plane is observed away from the FePt/MgO interface (A region) is in agreement with the previous works carried out by using XRD techniques.[7,15]

Figure 10 shows the inverse-FFT high resolution TEM image of FePt/VN/$SrTiO_3$(001) sample which is filtered in a similar way to that of Fig. 9. The (020) lattice images of VN and FePt are continuous and these layers are growing epitaxially on the $SrTiO_3$(001) substrate. Very small number of misfit dislocation is observed in FePt layer for the sample, though fairly large lattice mismatches exist between these materials (-7.1 %: $L1_0$-FePt/VN, 5.9 %: VN/$SrTiO_3$). A misfit dislocation observed in the VN layer is considered to have been introduced during the layer growth process to accommodate the lattice mismatch of 5.9 % with the base substrate. The (020) lattice line images in FePt layer are slightly bending along the film growth direction. Such lattice bending is considered to be due to a flexibility of very thin FePt layer with thickness of only 2 nm and the lattice bending is possibly absorbing the lattice mismatch of -7.1 %. For the material combination, the lateral strain in $A1$-FePt/VN/$SrTiO_3$(001) sample prepared at the low temperature of 200 °C is interpreted to be not high enough to enhance $L1_0$-ordering upon higher temperature annealing. The $L1_0$-ordering degree of 2-nm-thick FePt layer formed on VN underlayer is as low as 0.2, which may be attributed to a reduced lateral stress within the $A1$-FePt epitaxial thin film. To enhance $L1_0$-ordering, formation of MgO cap-layer is effective as reported in another paper.[21]

3.4 Nucleation and growth of $L1_0$-ordered crystal in FePt film

In the present study, a two-step process consisting of low temperature deposition at 200 °C followed by high temperature annealing at 600 °C is employed for preparation of $L1_0$-ordered FePt thin films. Form the structure analyses based on TEM observation for the FePt thin films of disordered $A1$ and of $L1_0$-ordered phases and also by considering the results reported in the references [7,8,15,19], it is possible to discuss the phase transformation from $A1$ to $L1_0$ phase based on nucleation and growth of $L1_0$-ordered crystal in disordered $A1$-FePt thin film.

(a) Structure of $A1$-FePt film with and without epitaxial cap-layer

When FePt film is formed on a substrate or underlayer of which lattice constant is slightly larger than that of $A1$-PePt, such as MgO(001), a lateral strain is induced and the lattice parameter of a_{FePt} is expanded

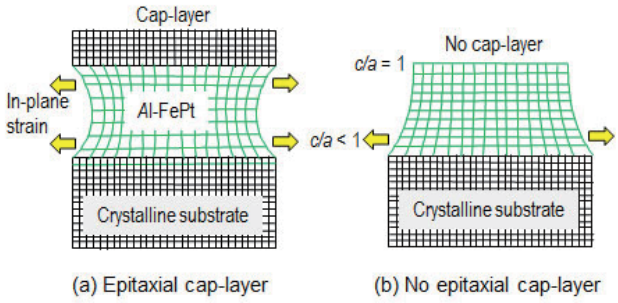

Fig. 11 Schematic model for epitaxial $A1$-FePt(001) film (a) with and (b) without cap-layer. Lateral strain is induced in $A1$-FePt epitaxial film by lattice mismatch with cap-layer and/or substrate.

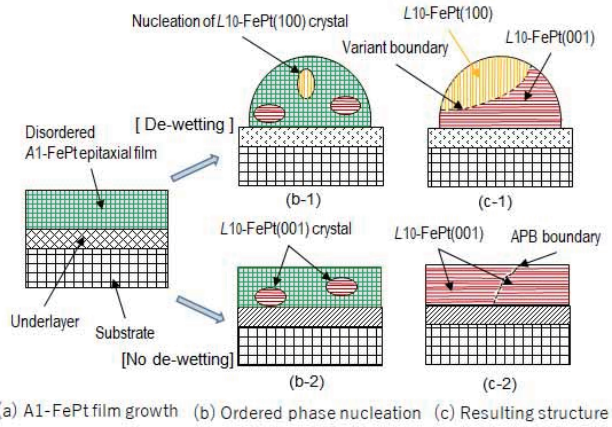

Fig. 12 Schematic model to explain the process of nucleation and growth of $L1_0$-crystal in $A1$-FePt(001) epitaxial film with different in-plane strain distributions.

schematically as illustrated in Fig. 11 (a). On the contrary for the FePt film without cap-layer, Fig. 11(b), the lateral strain decreases with increasing film thickness, which will induce free nucleation of $L1_0$-crystal in a region away from the substrate.

(b) Nucleation and growth of $L1_0$-ordered crystal

Figure 12 explains the process of nucleation and growth of $L1_0$-crystal in $A1$-FePt(001) film for two cases. One is the case where de-wetting of FePt material takes place when heated at a higher temperature for $L1_0$-ordering. In this case, isolated crystal islands are formed on the substrate, where the thickness is greatly increased due to condensation of FePt material. This case is observed for the 2-nm-thick FePt film formed on MgO(001) underlayer. The other is the case where the film morphology is kept during the higher temperature heating process, which is observed for the 2-nm-thick FePt film formed on VN(001) underlayer.

When de-wetting of FePt material takes place, in-plane strain distribution in FePt material will vary from the distribution in a flat and continuous $A1$-FePt film shown schematically in Fig. 11 (b). Although lateral strain is remaining in a region close to the substrate which is caused by the lattice mismatch with substrate, strain will be released in a region away from the substrate due to formation of rounded surface for the de-wetted island which is governed dominantly by the surface tension of FePt material. The increase of island thickness caused by FePt material condensation also reduces lateral strain by increasing the distance from substrate interface. As a result, the possibility of c-axis in-plane oriented $L1_0$-crystal nucleation will increase in regions away from the substrate as schematically shown in Fig. 12 (b-1). In a case of free nucleation in non-strained $A1$-FePt(001) film, the possibility of $L1_0$-(100), (010) crystal nucleation is 2/3, or 67 %. After crystal growth, the island will include variants of $L1_0$-FePt(100), (010) in addition to $L1_0$-FePt(001) variants, as shown in Fig. 12 (c-1).

In the case where de-wetting does not occur when heated at a higher temperature, the lateral strain in $A1$-FePt(001) film will be maintained. The nucleation of $L1_0$-(001) crystal with $c/a < 1$ is favored as shown in Fig. 12 (b-2), and hence a continuous $L1_0$-ordered film consisting of $L1_0$-(001) variants can be obtained, as indicated in Fig. 12 (c-2). In this case, anti-phase boundary, where two $L1_0$-(001) crystals with a half-lattice-length shifted along the c-axis each other are meeting, will be formed as the variant boundary. The variant diameter depends on the nucleation density of $L1_0$-crystal in $A1$-FePt(001) matrix, which is one of the important factors that determine the resulting $L1_0$-ordered thin film structure. The density varies depending on various parameters such as processing condition, substrate material, defect density of substrate, magnetic material composition, etc. From the studies of epitaxial magnetic thin films prepared on single-crystal substrates,[7,8,15,17,19] the average distance of $L1_0$-ordered FePt crystal nucleation is estimated to be less than 10 nm. A small distance less than 10 nm between two variants is observed in the present study (Fig. 9). Therefore, controlling of $L1_0$-crystal nucleation to be with the c-axis perpendicular to the substrate surface is particularly important for preparation of FePt thin films with larger thicknesses.

From the results and discussion of present study, the following conditions are deduced to be useful in aligning the c-axis to be perpendicular. (1) Employment of film thickness less than the average distance of $L1_0$-ordered crystal nucleation under a condition that the film is formed on a substrate which gives a lateral strain through lattice mismatch. (2) Use of a substrate material on which continuous morphology of FePt film can be kept during the high temperature processing for $L1_0$-ordering. The lateral strain in FePt film caused by the mismatch with substrate will be kept during $L1_0$-crystal nucleation process. (3) Formation of epitaxial cap-layer on FePt thin film in addition to a use of substrate material that gives lateral strain. (4) Increase of mechanical flexibility (lower Young's modulus) and increase of average distance of $L1_0$-crystal nucleation. By employing an Fe(Pt,Pd) magnetic material , for example, the Young's modulus and the nucleation density are expected to decrease. The melting temperature (1304 °C) and the Young's modulus (169 GPa) of FePd material[24] are lower than those of FePt (1500 °C, 237 GPa). It has been already made clear that $L1_0$-ordered FePd thin films can be prepared on MgO(001) substrates up to the thickness around 40 nm with the c-axis aligned perpendicular, and the volume fraction of c-axis in-plane oriented $L1_0$-variants can be decreased by increasing the Pd concentration in Fe(Pt.Pd)-alloy thin films.[7] Use of mixed alloy magnetic material will enhance the possibility of preparation of c-axis perpendicularly controlled epitaxial $L1_0$-ordered thin films. Adjustment of magneto-crystalline anisotropy energy (K_u) between the values of $L1_0$-FePt (6.6×10^7 erg/cm^3) and $L1_0$-FePd (1.8×10^7 erg/cm^3) [25] will be another advantage in applying the high-K_u magnetic thin films for future device applications.

4. Conclusions

Cross-sectional structures are observed by high-resolution transmission electron microscopy for FePt thin films epitaxially grown on (001) oriented substrates prepared by using a two-step process consisting of film formation at 200 °C followed by annealing at 600 °C for $L1_0$-ordering. The effects of epitaxial MgO cap-layer and (001) oriented substrates on the film structures are investigated and the nucleation and growth of

$L1_0$-ordered crystal in disordered $A1$-FePt thin film is discussed.

The $A1$-FePt crystal lattice of MgO (2 nm)/$A1$-FePt (10 nm)/MgO(001) sample is expanded in the parallel direction to the substrate surface in accommodation of lattice mismatch with the substrate and the cap-layer, and a variation of lattice parameter (a_{FePt}) along the film growth direction is recognized. The crystal lattice of $A1$-FePt film is strained in lateral direction though misfit dislocations exist in the $A1$-FePt film near the interfaces.

The FePt film in a sample of $L1_0$-FePt(2 nm)/VN(001)(2 nm)$_{underlayer}$ was consisting of one type of $L1_0$-variant, FePt(001), whereas the FePt film in a $L1_0$-FePt(2-nm average thickness)/MgO(001)(2 nm)$_{underlayer}$ sample included variants of $L1_0$(100),(010) with the c-axis lying in-plane in addition to $L1_0$(001) variant with the c-axis perpendicular. The lattice mismatch with the substrate is reduced by introduction of misfit dislocation and by lattice bending of FePt crystal. The variant structures are interpreted to be influenced by the lattice strain of $A1$-FePt film during the nucleation stage at the high temperature annealing process.

Based on the experimental results, a model to explain the phase transformation from disordered $A1$ to ordered $L1_0$ involving nucleation and growth of $L1_0$-crystal in A1-FePt film is proposed.

Acknowledgment The work was supported by the Chuo University Grant for Special Research.

References

1) R. F. C. Farrow, D. Weller, R. F. Marks, and M. F. Toney, *Appl. Phys. Lett.*, **69**, 1166 (1996).
2) J. S. Chen, Yingfan Xu, and J. P. Wang, *J. Appl. Phys.*, **93**, 1661 (2003).
3) L. J. Zhang, J. W. Cai, and H. Y. Pan, *J. Appl. Phys.*, **102**, 013905 (2007).
4) T. Suzuki, N. Honda, and K. Ouchi, *J. Appl. Phys.*,**85**, 4301, (1999).
5) K. F. Dong, H. H. Li, and J. S. Chen, *J. Appl. Phys.*, **113**, 233904 (2013).
6) C. Feng, E. Zhang, C. C. Xu, N. Li, Y. Jiang, G. H. Yu, and B. H. Li, *J. Appl. Phys.* **110**, 063910 (2011).
7) M. Futamoto, M. Nakamura, M. Ohtake, N. Inaba, and T. Shimotsu, *AIP Adv.*, **6**, 085302 (2016).
8) M. Nakamura, R. Ochiai, M. Ohtake, M. Futamoto, F. Kirino, and N. Inaba, *IEICE Tech. Rep.*, **116**, MR2016-14, pp. 13, 2016.
9) K. Sato, B. Bian, T. Hanada, and Y. Hirotsu, *Scripta Mater.*, **44**, 1389 (2001).
10) T. Shima, K. Takanashi, Y. K. Takahashi, and K. Hono, *Appl. Phys. Lett.*, **81**, 1050 (2002).
11) Y. Hirotsu and K. Sato, *J. Cer. Proc. Res.*, **6**, 236 (2005).
12) Y. Fuji, T. Miyazaki, S. Okamoto, O. Kitakami, Y. Shimada, and J. Koike, *J. Magn. Soc. Jpn.*, **28**, 376 (2004).
13) T. Suzuki and K. Ouchi, *J. Appl. Phys.*, **91**, 8079 (2002).
14) A. Itabashi, M. Ohtake, S. Ouchi, F. Kirino, and M. Futamoto, *IEEE Trans. Magn.*, **48**, 3203 (2012).
15) M. Ohtake, A. Itabashi, M. Futamoto, F. Kirino, N. Inaba, *J. Magn. Soc. Jpn.*, **39**, 167 (2015).
16) T. Shimizu, M. Ohtake, M. Futamoto, F. Kirino, and N. Inaba, *IEEE Trans. Magn.*, **53,** 2101904 (2017).
17) J-W Liao, K-F Huang, L-W Wang, W-C Tsai, W-C Wen, C-C Chiang, H-J Lin, F-H Chang, and C-H Lai, *Appl. Phys. Lett.*, **102**, 062420 (2013).
18) A. T. McCallum, D. Kercher, J. Lille, D. Weller, and O. Hellwig, *Appl. Phys. Lett.,* **101**, 092402 (2012).
19) Y. Noguchi, M. Ohtake, M. Futamoto, F. Kirino, and N. Inaba, *J. Mag. Mag. Mater.*, **410**, 81 (2016).
20) M. Ohtake, M. Nakamura, M. Futamoto, F. Kirino, and N. Inaba, *AIP Adv.*, **7**, 056320 (2017).
21) T. Shimizu, M. Ohtake, M. Futamoto, F. Kirino, and N. Inaba, *Digest 41st Annual Conf. Mag. Japan.*, 21pB-9 (21, Sept. 2017).
22) B. Laenens, F. M. Almeida, N. Planckaert, K. Temst, J. Meersschaut, A. Vantomme, C. Rentenberger, M. Rennhofer, and B. Sepiol, *J. Appl. Phys.*, **105**, 073913 (2009).
23) S. Wicht, S. H. Wee, O. Hellwig, V. Mehta, S. Jain, D. Weller, and B. Rellinghaus, *J. Appl. Phys.,* **119**, 115301 (2016).
24) A. A. Al Ghaferi, *PhD Thesis "Deformation and Dislocation TEM Image Simulation in $L1_0$-FePd"*, (University of Pittsburgh, 2006).
25) J. M. D. Coey, *Magnetism and Magnetic Materials* (Cambridge Univ. Press, 2011).

Received Oct. 24, 2017; Revised Mar. 26, 2018; Accepted Jul. 11, 2018

J. Magn. Soc. Jpn., **42**, 110-118 (2018)

<Paper>

Writing Field Sensitivity in Heat-Assisted Magnetic Recording

T. Kobayashi, Y. Nakatani*, and Y. Fujiwara

Graduate School of Engineering, Mie Univ., *1577 Kurimamachiya-cho, Tsu 514-8507, Japan*

*Graduate School of Informatics and Engineering, Univ. of Electro-Communications, *1-5-1 Chofugaoka, Chofu 182-8585, Japan*

Work on increasing writing field sensitivity can be divided into four problems with some related calculation parameters when we consider the physical implications of applying our model calculation to heat-assisted magnetic recording. The four problems are write-error, erasure-after-write, statistics, and damping constant. The dependence of the bit error rate on writing field is calculated for various calculation parameters. As a result of optimization after considering the four problems, when the Gilbert damping constant is 0.1, writing is easy since the attempt period is short. A writing field of about 8 kOe is necessary if we are to realize 4 Tbpsi and a linear velocity of 10 m/s. On the other hand, when the damping constant is 0.01, writing is difficult since the attempt period is long. We need a writing field of about 13 kOe to achieve 2 Tbpsi and a linear velocity of 5 m/s under the conditions used in this study.

Key words: heat-assisted magnetic recording, field sensitivity, write-error, erasure-after-write, statistics, damping constant

1. Introduction

Heat-assisted magnetic recording (HAMR) is a promising candidate as a next generation magnetic recording method beyond the trilemma limit[1].

We have already proposed a new HAMR model calculation[2)~4)]. We have also improved our model calculation considering the temperature dependence of the attempt frequency. In addition, we have shown in our model calculation that the signal-to-noise ratio derived by the conventionally used micromagnetic calculation can be explained using the temperature dependences of the grain magnetization reversal probability and the attempt period, whose inverse is the attempt frequency[5]. Furthermore, since the calculation time of our model is short, we can quickly calculate the bit error rate (bER) using 10^5 or 10^6 bits. bER data are useful for determining whether or not recording is possible.

Since HAMR is a writing method in which the medium is heated to reduce coercivity at the time of writing, the coercivity of the medium can be reduced by any amount. However, micromagnetic simulation has shown that a relatively high writing field is necessary[6].

In this study, we discuss the writing field sensitivity with a view to improving HAMR design employing our improved model calculation[5]. A feature of our model calculation is that the interpretation of the result and the establishment of an HAMR design policy are easy. As a result of this study, we can divide the goal of increasing the writing field sensitivity into four problems considering the physical implications. The four problems are write-error[2], erasure-after-write[2], statistics, and damping constant[3]. The statistics problem is a problem related to the grain number per bit.

2. Calculation Method

2.1 Calculation conditions

The area S of one bit is 161 or 323 nm^2 for a recording density of 4 or 2 Tbpsi, respectively. The medium was assumed to be granular. The writing field switching timing and the calculation conditions are summarized in Fig. 1 for a $m \times n = 4 \times 1$ grain arrangement where m and n are the grain numbers in one bit for the cross-track and down-track directions, respectively. H_w and $\tau_{min} = D_{BP}/v$ are the writing field and the minimum magnetization transition time, respectively. The H_w direction is upward when $0 \le t < \tau_{min}$, and downward when $t < 0$ and $t \ge \tau_{min}$. When t = 0, the writing grain temperature T becomes T_c.

The mean grain size D_m was determined by

$$D_m = \sqrt{\frac{S}{mn}} - \Delta \qquad (1)$$

where Δ = 1 nm is the non-magnetic spacing. The track and bit pitches were $D_{TP} = m(D_m + \Delta)$ and $D_{BP} = n(D_m + \Delta)$, respectively, and then $S = D_{TP} \cdot D_{BP}$. The standard deviation of the grain size σ_D / D_m and the grain height h were 10 % and 8 nm, respectively, and so the grain volume V_m for D_m was $D_m \times D_m \times h$.

The medium was characterized by (1) the Curie temperature T_c, (2) the Gilbert damping constant α, and (3) the anisotropy constant ratio K_u / K_{bulk}, which is the intrinsic ratio of the medium anisotropy constant K_u to bulk FePt K_u[7].

(1) If T_c is low, a higher K_u / K_{bulk} is necessary[8]. Therefore, we chose a T_c value of 700 K. The standard deviation of the Curie temperature σ_{Tc} / T_c was assumed to be 0 %.

(2) The α value of FePt just below T_c is unknown. Therefore, we calculated the bit error rate using α = 0.1 and 0.01.
(3) The K_u / K_{bulk} value must be larger than the value required for 10 years of archiving.

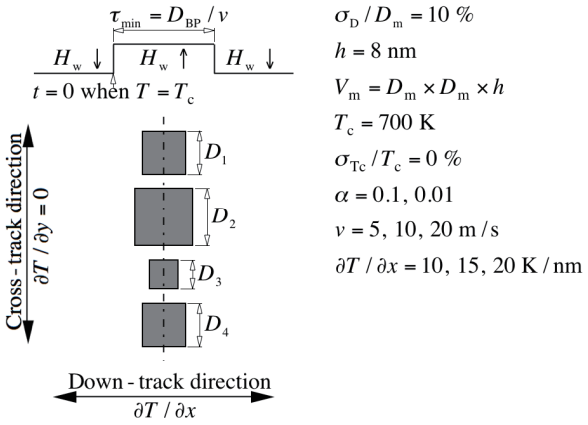

Fig. 1 Writing field switching timing and calculation conditions

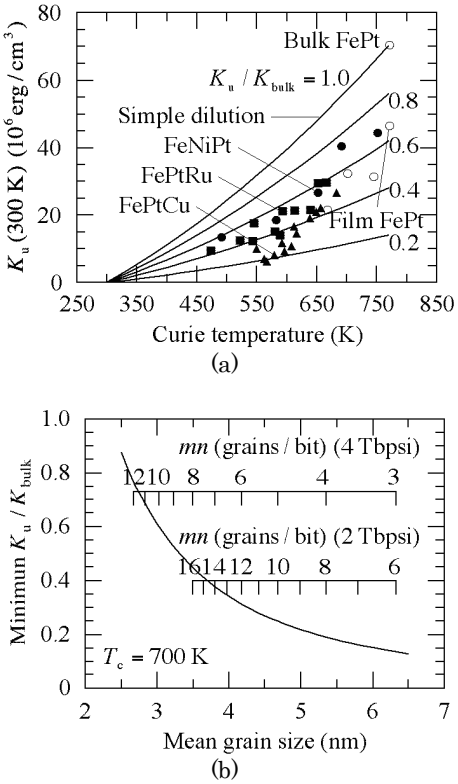

Fig. 2 (a) Dependence of anisotropy constant K_u on Curie temperature for various anisotropy constant ratios K_u / K_{bulk} and experimental results for film FePt[9),10)], FeNiPt[9)], FePtRu[10)], and FePtCu[10)], and (b) minimum K_u / K_{bulk} value for 10 years of archiving as a function of mean grain size.

The dependence of the anisotropy constant K_u for an FePt system on the Curie temperature is shown in Fig. 2 (a), where the solid lines show the simple diluted K_u values calculated with a mean field analysis for various K_u / K_{bulk} values.

The experimental results for FeNiPt[9)] and FePtRu[10)] films are on the simple dilution line, and those for FePtCu[10)] films are away from the line. Even good experimental results, namely those for FeNiPt[9)] and FePtRu[10)] films, are between K_u / K_{bulk} = 0.4 to 0.6.

Figure 2 (b) shows the minimum K_u / K_{bulk} value for 10 years of archiving as a function of the mean grain size. The inserted scales indicate the grain number per bit mn corresponding to the mean grain size for recording densities of 4 and 2 Tbpsi.

The minimum K_u / K_{bulk} value was roughly estimated using

$$\frac{K_u (300\ \mathrm{K}) V_m}{kT} > 60 \qquad (2)$$

where k and T are the Boltzmann constant and temperature, respectively. A method for calculating the numerical value instead of "60" on the right side in Eq. (2) has been proposed in previous papers[11),12)].

The calculation parameters were α, K_u / K_{bulk}, the linear velocity v, the thermal gradient $\partial T / \partial x$ for the down-track direction, the grain column number in one bit n, and the grain number per bit mn. The thermal gradient $\partial T / \partial y$ for the cross-track direction was assumed to be 0 K/nm.

2.2 Bit error rate calculation

The magnetization direction of the grains was calculated using the magnetization reversal probability for every attempt time in our model calculation[2)~5)].

The probability P_- for each attempt where the magnetization M_s and the writing field H_w change from antiparallel to parallel is expressed as

$$P_- = \exp\left(-K_{\beta-}\right). \qquad (3)$$

On the other hand,

$$P_+ = \exp\left(-K_{\beta+}\right) \qquad (4)$$

is the probability for each attempt where M_s and H_w change from parallel to antiparallel. In these equations,

$$K_{\beta-}(T, H_w) = \frac{K_u(T) V}{kT}\left(1 - \frac{H_w}{H_k(T)}\right)^2 \quad \left(H_k(T) \geq H_w\right),$$

$$K_{\beta-}(T, H_w) = 0 \quad \left(H_k(T) < H_w\right), \qquad (5)$$

and

$$K_{\beta+}(T, H_w) = \frac{K_u(T) V}{kT}\left(1 + \frac{H_w}{H_k(T)}\right)^2, \qquad (6)$$

where K_u, V, k, T, and $H_k = 2K_u/M_s$ are the anisotropy constant, the grain volume, the Boltzmann constant, temperature, and the anisotropy field, respectively.

The temperature dependence of M_s was determined employing a mean field analysis[13], and that of K_u was assumed to be proportional to M_s^2 [9]. The Curie temperature T_c was adjusted by the Cu simple dilution of $(Fe_{0.5}Pt_{0.5})_{1-z}Cu_z$. $M_s(T_c, T)$ is a function of T_c and T. $M_s(T_c = 770\ \mathrm{K}, T = 300\ \mathrm{K}) = 1000$ emu/cm^3 was assumed. $K_u(T_c, K_u/K_{bulk}, T)$ is a function of T_c, the anisotropy constant ratio K_u/K_{bulk}, and T. $K_u(T_c = 770\ \mathrm{K}, K_u/K_{bulk} = 1, T = 300\ \mathrm{K}) = 70$ Merg/cm^3 was assumed. We used $M_s(T_c = 700\ \mathrm{K}, T)$ and $K_u(T_c = 700\ \mathrm{K}, K_u/K_{bulk}, T)$ for the calculations in this paper.

On the other hand, an attempt time t_k, whose interval is an attempt period τ_{AP}, is determined in the following[5]. The inverse of the attempt period is an attempt frequency $f_0 = 1/\tau_{AP}$. Since there was a very good linear relationship between f_0 and T, we used

$$f_0(T) = \frac{2a\alpha}{1+\alpha^2}\sqrt{\frac{V}{V_0}}\frac{K_u/K_{bulk}}{0.4}(T_c - T) \qquad (7)$$

where $a = 5$ (nsK)$^{-1}$ and $V_0 = 193$ nm^3. The f_0 value becomes zero at $T = T_c$ as shown in Eq. (7).

We defined an initial time t_{ini1} at $T = T_{th} = 699$ K, which is close to $T_c = 700$ K, using

$$t_{ini1} = \frac{T_c - T_{th}}{v(\partial T/\partial x)} \qquad (8)$$

since $\tau_{AP} = 1/f_0$ diverges to infinity at $T = T_c$. The next initial time t_{ini2} was calculated using the mean attempt period τ_{APm} from t_{ini1} to t_{ini2} expressed by

$$t_{ini2} - t_{ini1} = \tau_{APm} = \frac{1}{t_{ini2} - t_{ini1}}\int_{t_{ini1}}^{t_{ini2}} \tau_{AP}(t)dt\,. \qquad (9)$$

We assumed that the first attempt time t_1 is randomly decided between t_{ini1} and t_{ini2}. And the attempt time t_{k+1} $(k \geq 1)$ is determined with the following recurrence formula:

$$t_{k+1} - t_k = \tau_{APm} = \frac{1}{t_{k+1} - t_k}\int_{t_k}^{t_{k+1}} \tau_{AP}(t)dt\,. \qquad (10)$$

The writing field was assumed to be spatially uniform, the direction was perpendicular to the medium plane, and the rise time was zero. Neither the demagnetizing nor the magnetostatic fields were considered during writing since they are negligibly small.

Errors occur in some grains of a bit. We assume that if the magnetic pole of the grains where the magnetization turns in the recording direction $\sum M_{ij}D_{ij}^2$ is more than 50 % of the total mean magnetic pole $mn \cdot M_s D_m^2$ in one bit, the bit is error free. Namely, if

$$\frac{\sum_{i,j} M_{ij}D_{ij}^2}{mn \cdot M_s D_m^2} > 0.5, \qquad (11)$$

the bit is error free. The number of calculation bits is 10^5. A criterion determining whether or not recording is possible was assumed to be a bit error rate (bER) of 10^{-3}. Increasing the writing field sensitivity means lowering the writing field at which the bER value is 10^{-3}. The bER in this study is useful only for a comparison.

The calculation procedure is described below. First, the medium was characterized by $T_c = 700$ K, α, and K_u/K_{bulk}. The grain temperature fell with time from T_c according to the linear velocity v and the thermal gradient $\partial T/\partial x$ for the down-track direction. The attempt times were calculated. The magnetic property and then $P_{\pm}$ were calculated by undertaking a mean field analysis for every attempt time. The magnetization direction was determined by the Monte Carlo method for every attempt time. Then the bER was obtained.

3. Calculation Results

As a result of this study, we can divide the goal of increasing the writing field sensitivity into four problems with some related calculation parameters considering the physical implications. The four problems and the main related parameters are summarized below.

(1) Write-error problem

The main related parameters are the anisotropy constant ratio K_u/K_{bulk} and the linear velocity v.

(2) Erasure-after-write problem

The K_u/K_{bulk} value, the thermal gradient $\partial T/\partial x$ for the down-track direction, and the grain column number in one bit n.

(3) Statistics problem

The grain number per bit mn.

(4) Damping constant α problem

3.1 Write-error problem

The main related parameters in the write-error problem are the anisotropy constant ratio K_u/K_{bulk} and the linear velocity v.

First, we deal with K_u/K_{bulk} for the damping constant $\alpha = 0.1$. Figure 3 (a) shows the dependence of bit error rate (bER) on writing field H_w for various K_u/K_{bulk} values where the recording density, grain number mn, and mean grain size D_m are 4 Tbpsi, 4, and 5.4 nm, respectively, and there is a 4×1 grain arrangement. The decrease and increase in bER as H_w increases are caused by a reduction in the write-error (WE) and an increase in erasure-after-write (EAW)[6], respectively. EAW must be sufficiently low in a low writing field region to achieve a low bER. Large dependences of WE and EAW on K_u/K_{bulk} can be seen.

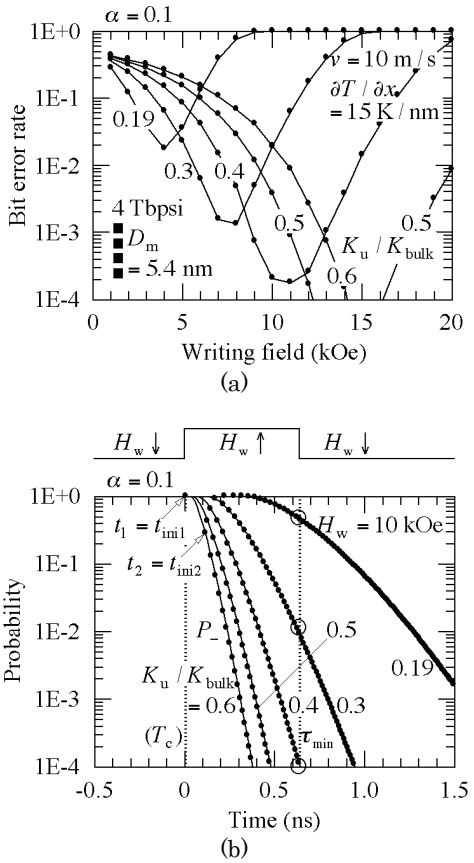

Fig. 3 (a) Dependence of bit error rate on writing field for various anisotropy constant ratios K_u/K_{bulk} (4 Tbpsi), and (b) time dependence of grain magnetization reversal probability P_- for various K_u/K_{bulk} values.

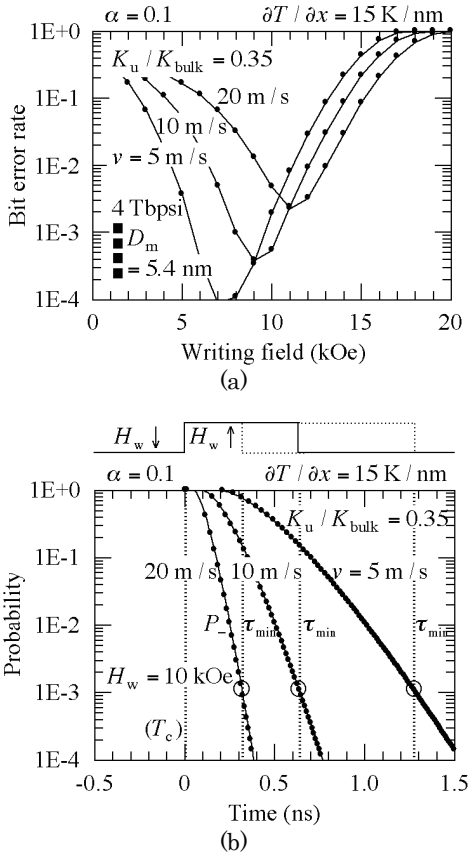

Fig. 4 (a) Dependence of bit error rate on writing field for various linear velocities v (4 Tbpsi), and (b) time dependence of grain magnetization reversal probability P_- for various v values.

Reducing K_u/K_{bulk} is effective in reducing WE, namely, in increasing the writing field sensitivity. Although the coercivity can be reduced by any amount during writing in HAMR, a higher H_w is necessary for a higher K_u/K_{bulk}, namely, for a higher coercivity. This is explained using the time dependence of the grain magnetization reversal probability P_- for various K_u/K_{bulk} values at H_w = 10 kOe as shown in Fig. 3 (b). P_- is rapidly decreased after 0 ns according to Eqs. (3) and (5) since the temperature decreases with time. The filled circles indicate the attempt times t_k whose interval is the mean attempt period τ_{APm}. This paper includes figures showing P_- with time for $t_1 = t_{ini1}$ and $t_2 = t_{ini2}$. The time t = 0 is the onset of the writing time, which corresponds to the writing grain temperature becoming the Curie temperature T_c. The attempt frequency f_0 is low just below T_c as shown in Eq. (7), and then the attempt period $\tau_{AP} = 1/f_0$ is long just after t = 0. The temperature decreases with time, and τ_{AP} decreases accordingly. Therefore, τ_{APm} decreases with time. $t = \tau_{min}$ is the end of the writing time, which corresponds to the minimum magnetization transition time and $\tau_{min} = D_{BP}/v$ as shown in Fig. 1.

WE occurs during writing ($0 \le t < \tau_{min}$)[2], and the attempt number is important when P_- is high and $0 \le t < \tau_{min}$. The attempt numbers are about 15, 12, 7, 4, and 3 for K_u/K_{bulk} = 0.19, 0.3, 0.4, 0.5, and 0.6, respectively, when $0.1 \le P_- \le 1$ and $0 \le t < \tau_{min}$ at H_w = 10 kOe as shown in Fig. 3 (b). Since the dependence of the attempt number on K_u/K_{bulk} is large, reducing K_u/K_{bulk} is effective in decreasing WE as shown in Fig. 3 (a).

The anisotropy constant ratio is also the main related parameter for EAW. The large dependence of EAW on K_u/K_{bulk} as shown in Fig. 3 (a) will be discussed in **3.2**.

When we consider WE and EAW in Fig. 3 (a), a K_u/K_{bulk} value of about 0.35 is the best condition for 4 Tbpsi and a 4×1 grain arrangement even though the minimum K_u/K_{bulk} value for 10 years of archiving is 0.19 as shown in Fig. 2 (b).

Next, we discuss the linear velocity v in the write-error problem for α = 0.1 and K_u/K_{bulk} = 0.35. Figure 4 (a) shows the dependence of bER on writing field H_w for various v values. A large WE dependence and a small EAW dependence on v can be seen. This is also explained using the time dependence of the grain magnetization reversal probability P_- as shown in Fig. 4 (b). The τ_{min} values are 1.27, 0.64, and

0.32 ns for v = 5, 10, and 20 m/s, respectively. The attempt numbers are about 18, 9, and 4 for v = 5, 10, and 20 m/s, respectively, when $0.1 \le P_{-} \le 1$. Since the dependence of the attempt number on v is large, reducing v is effective in decreasing WE.

On the other hand, EAW is the grain magnetization reversal in the opposite direction to the recording direction caused by changing the H_w direction at the end of the writing time τ_{min}. Therefore, EAW occurs after writing ($t \ge \tau_{min}$)[2], and the P_{-} value at the end of the writing time τ_{min} is important. The temperatures at τ_{min} are the same regardless of the v values since the thermal gradient is constant. Then, the P_{-} values at τ_{min} are the same regardless of the v values designated by the open circles in Fig. 4 (b). Therefore, the EAW dependence on v is small, and the linear velocity is not the main related parameter for EAW.

3.2 Erasure-after-write problem

The main related parameters in the erasure-after-write problem are the K_u/K_{bulk} value, the thermal gradient $\partial T/\partial x$ for the down-track direction, and the grain column number in one bit n.

In this section, we first discuss K_u/K_{bulk} for α = 0.1. A large erasure-after-write (EAW) dependence on K_u/K_{bulk} can be seen in Fig. 3 (a). If the P_{-} values at τ_{min} designated by the open circles in Fig. 3 (b) are insufficiently low, EAW occurs. The P_{-} value abruptly decreases as K_u/K_{bulk} increases. Therefore, increasing K_u/K_{bulk} is effective in reducing EAW as shown in Fig. 3 (a).

Next, the thermal gradient $\partial T/\partial x$ in the erasure-after-write problem is discussed for α = 0.1 and K_u/K_{bulk} = 0.35. Figure 5 (a) shows the dependence of bit error rate (bER) on the writing field H_w for various $\partial T/\partial x$ values. A large EAW dependence and a small WE dependence on $\partial T/\partial x$ can be seen. As mentioned above, the magnetization reversal probability P_{-} at τ_{min} is important for EAW, and the P_{-} values at τ_{min} designated by the open circles in Fig. 5 (b) are reduced as $\partial T/\partial x$ increases. Therefore, increasing $\partial T/\partial x$ is effective in reducing EAW as shown in Fig. 5 (a).

On the other hand, the attempt number is important for WE when P_{-} is high. The attempt numbers are about 13, 9, and 6 for $\partial T/\partial x$ = 10, 15, and 20 K/nm, respectively, when $0.1 \le P_{-} \le 1$ as shown in Fig. 5 (b). Since the dependence of the attempt number on $\partial T/\partial x$ is small, the dependence of WE on $\partial T/\partial x$ is small as shown in Fig. 5 (a), and the thermal gradient is not the main related parameter for WE.

Finally, in this section, the grain column number in the erasure-after-write problem is discussed for α = 0.1 and K_u/K_{bulk} = 0.35. We performed a comparison regarding the grain column number in one bit n. Figure 6 (a) shows the dependence of bER on the writing field H_w for n = 2 (4 Tbpsi, 2×2) and n = 1 (4 Tbpsi, 4×1 grain arrangement). The dotted lines show the bER values for n = 1. It is characteristic that the bER values caused by WE are the same and the bER caused by EAW for n = 2 is lower than that for n = 1.

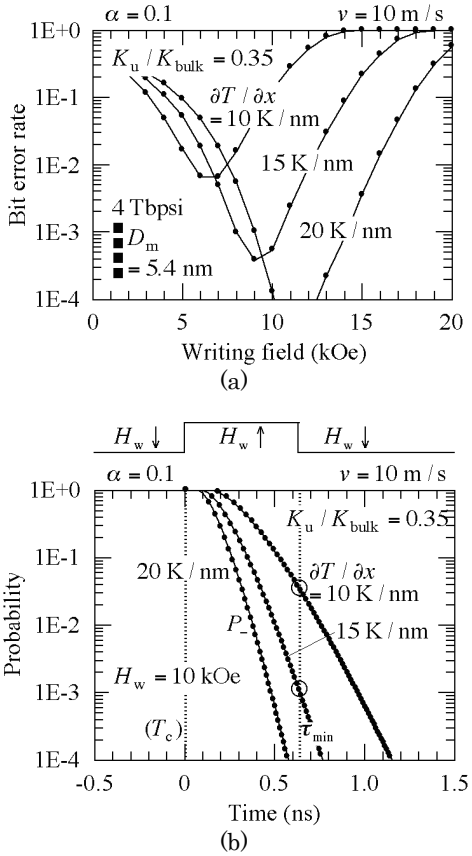

Fig. 5 (a) Dependence of bit error rate on writing field for various thermal gradients $\partial T/\partial x$ (4 Tbpsi), and (b) time dependence of grain magnetization reversal probability P_{-} for various $\partial T/\partial x$ values.

This is explained using the time dependence of the grain magnetization reversal probability P_{-} for n = 2 as shown in Fig. 6 (b) at H_w = 10 kOe and (c) H_w = 15 kOe. The times corresponding to the Curie temperatures T_{c1} and T_{c2} are 0 and 0.64 ns for the 1st and 2nd columns, respectively, and the end of the writing time τ_{min} is 1.27 ns. The attempt numbers are the same for the 1st and 2nd columns when $0.1 \le P_{-} \le 1$ as shown in Fig. 6 (b). Therefore, the bER values caused by WE are the same for the 1st and 2nd columns, and the grain column number in one bit is not the related parameter for WE.

The writing times, which are the times corresponding to T_{c1} and T_{c2} to τ_{min}, are 1.27 and 0.64 ns for the 1st and 2nd columns as shown in Fig. 6 (c), respectively. Since the writing time is long in the 1st column, P_{-} at τ_{min} is sufficiently low and EAW does not occur even at H_w = 15 kOe. However, the writing time is only 0.64 ns in the 2nd column. Therefore, EAW occurs only in the 2nd column since P_{-} at τ_{min} denoted by an open circle is insufficiently low only for the 2nd column.

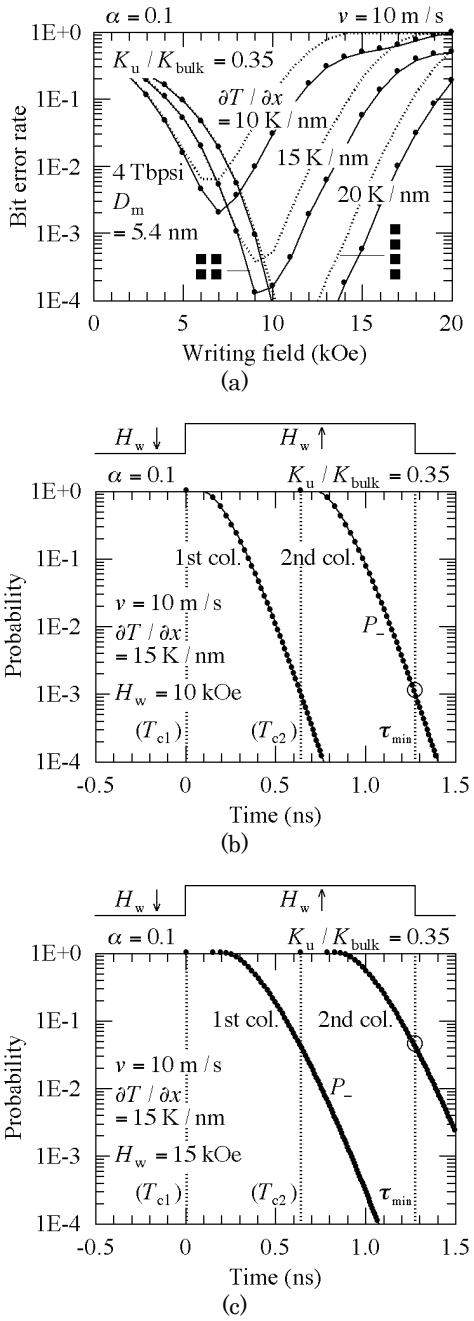

Fig. 6 (a) Dependence of bit error rate on writing field H_w for grain column numbers n = 2 and 1 (4 Tbpsi), (b) time dependence of grain magnetization reversal probability P_- for n = 2 at H_w = 10 kOe, and (c) H_w = 15 kOe.

The increase in the grain column number under a constant recording density is effective for achieving a wide writing field margin, namely a wide writing field region where the bER value is less than 10^{-3}.

3.3 Statistics problem

In this section, we discuss the grain number in the statistics problem for α = 0.1. We performed a comparison regarding the grain number per bit mn. Figures 7 (a) and (b) show the dependence of bit error rate (bER) on the writing field H_w for mn = 4 (4 Tbpsi, 2×2) and mn = 8 (2 Tbpsi, 4×2 grain arrangement) where the mean grain sizes D_m for mn = 4 and 8 are the same. The bER value for mn = 8 is lower than that for mn = 4. Since the calculation conditions except the grain row number m are the same, the WE probabilities are the same in Figs. 7 (a) and (b). Furthermore, since the grain column numbers in one bit n are the same, the EAW probabilities are also the same in Figs. 7 (a) and (b). Therefore, the reason for the bER difference is a statistics problem.

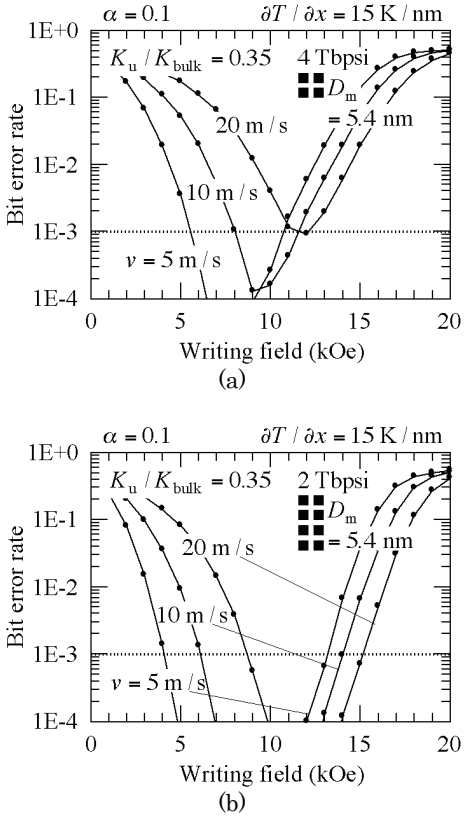

Fig. 7 Dependence of bit error rate on writing field for (a) grain numbers mn = 4 (4 Tbpsi) and (b) mn = 8 (2 Tbpsi).

Statistics problem is explained using the following example. All grains are assumed to be homogeneous. When the grain error probability p is 0.1, the bER value for mn = 4 is calculated as

$$\mathrm{bER} = \sum_{k=2}^{4} {}_4C_k p^k (1-p)^{4-k} \approx 0.05. \qquad (12)$$

On the other hand, the bER value for mn = 8 is

$$\mathrm{bER} = \sum_{k=4}^{8} {}_8C_k p^k (1-p)^{8-k} \approx 0.005, \qquad (13)$$

which is much lower than that for mn = 4 in Eq. (12).

If one bit contains many grains, the bER becomes low since the probability is very low for a simultaneous error for more than half of the grains in one bit.

Therefore, even if the grain error probability, namely, the WE or EAW probability, does not change, increasing the grain number under a constant mean grain size is effective in reducing the bER for a statistical reason.

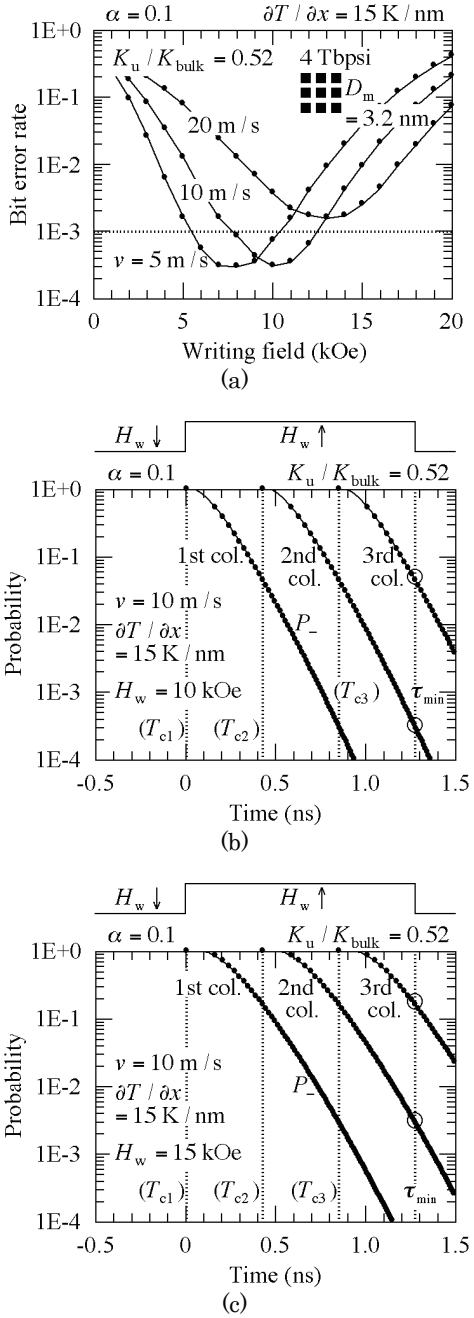

Fig. 8 (a) Dependence of bit error rate on writing field H_w for grain number mn = 9 (4 Tbpsi), (b) time dependence of grain magnetization reversal probability P_- for mn = 9 at H_w = 10 kOe, and (c) H_w = 15 kOe.

The difference between the calculation conditions in Figs. 7 (a) and (b) is only the grain row number or the recording density, and the mean grain sizes are the same. Next, we discuss the case where the recording densities are the same and the mean grain sizes D_m are different. When 4 Tbpsi and mn = 4 (2×2 grain arrangement), a writing field H_w of about 8 kOe is necessary for bER = 10^{-3} and the linear velocity v = 10 m/s as shown in Fig. 7 (a) where D_m = 5.4 nm and K_u/K_{bulk} = 0.35. Figure 8 (a) shows the dependence of bER on H_w for 4 Tbpsi and mn = 9 (3×3 grain arrangement) where the D_m value is 3.2 nm and K_u/K_{bulk} is increased to a minimum value of 0.52 for 10 years of archiving. An H_w value of about 8 kOe is also necessary for bER = 10^{-3} and v = 10 m/s. Although the mn and n numbers in Fig. 8 (a) are larger than those in Fig. 7 (a), the writing field sensitivities for bER = 10^{-3} are almost the same.

Figures 8 (b) and (c) corresponding to Figs. 6 (b) and (c), respectively, show the time dependence of the grain magnetization reversal probability P_-. The first difference between the calculation conditions in Figs. 8 and 6 is the writing time. The writing times are 1.27, 0.85, and 0.42 ns, respectively, for the 1st, 2nd, and 3rd columns as shown in Fig. 8. The writing time of the 3rd column in Fig. 8 is shorter than that of the 2nd column in Fig. 6. The second difference is the rate at which P_- decreases with time according to Eq. (5), in which K_u, V, and $H_k = 2K_u/M_s$, namely K_u/K_{bulk} and D_m are the different parameters.

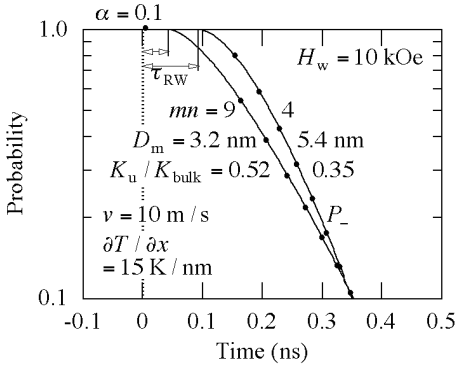

Fig. 9 Time dependence of grain magnetization reversal probability P_- for mn = 9 and 4 (4 Tbpsi) at H_w = 10 kOe.

Figure 9 shows the comparison of P_- for mn = 9 (D_m = 3.2 nm and K_u/K_{bulk} = 0.52) and 4 (D_m = 5.4 nm and K_u/K_{bulk} = 0.35). The third difference is the recording time window[6] τ_{RW} where τ_{RW} is a time for P_- = 1, namely $H_k < H_w$ according to Eq. (5). The recording time window τ_{RW} for mn = 9 is shorter than that for mn = 4 as shown in Fig. 9 since K_u/K_{bulk} for mn = 9 is higher than that for mn = 4. The fourth difference is the attempt frequency f_0 according to Eq. (7), in which V and K_u/K_{bulk}, namely D_m and K_u/K_{bulk} are the different parameters. The attempt period $\tau_{AP} = 1/f_0$ for mn = 9 is somewhat longer than that for mn = 4 as shown in Fig. 9 since $D_m \cdot K_u/K_{bulk}$ for mn = 9 is somewhat smaller than that for mn = 4.

Although we can expect an increase in the writing field sensitivity owing to the small reduction rate of P_{-} with time and a statistical effect, the writing field sensitivities are almost the same in Figs. 7 (a) and 8 (a) since the recording time window decreases and the attempt period increases as the grain number mn increases.

Although the P_{-} value of the 2nd column at τ_{min} indicated by an open circle in Fig. 6 (b) is sufficiently low, that of the 3rd column in Fig. 8 (b) is insufficiently low even at H_w = 10 kOe. Furthermore, although the P_{-} value of the 1st column at τ_{min} in Fig. 6 (c) is less than 10^{-4}, that of the 2nd column shown by an open circle in Fig. 8 (c) is more than 10^{-3} at H_w = 15 kOe. Therefore, although the grain column number n increases and there is a statistical effect, the bER value caused by EAW is also scarcely changed by increasing n and mn.

The writing properties are almost the same regardless of the grain number per bit under a constant recording density. However, there are fluctuations in the switching timing Δt and position Δx in a granular medium[3], and it is assumed that increasing the grain number is advantageous as regards suppression of the bER degradation caused by the fluctuations in Δt and Δx. This is a subject for future study.

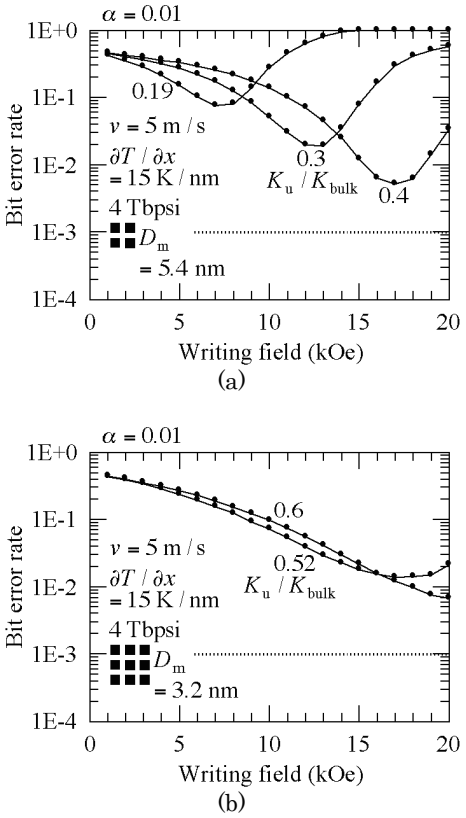

Fig. 10 Dependence of bit error rate on writing field for (a) grain numbers mn = 4 (4 Tbpsi) and (b) mn = 9 (4 Tbpsi) where damping constant α = 0.01.

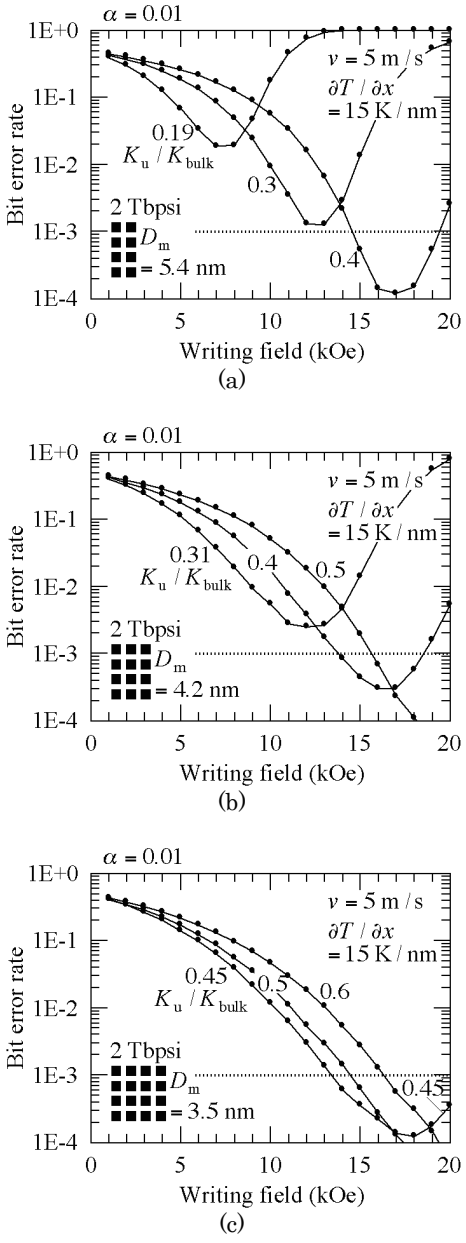

Fig. 11 Dependence of bit error rate on writing field for (a) grain numbers mn = 8 (2 Tbpsi), (b) mn = 12 (2 Tbpsi), and (c) mn = 16 (2 Tbpsi) where damping constant α = 0.01.

3.4 Damping constant problem

Finally, this section considers the damping constant problem since the damping constant of FePt just below the Curie temperature is unknown. In a previous paper[5], we used the signal-to-noise ratio to show that if the damping constant is small, the write-error (WE) is dominant and writing is difficult since the attempt period is long and there is almost no opportunity for writing. We discuss this problem using the bit error rate (bER) value for the damping constant α = 0.01 instead of 0.1 where the attempt period is about ten times longer. Since WE is dominant and writing is difficult, we used the K_u/K_{bulk} values including the minimum K_u/K_{bulk} value and a slow linear velocity of

5 m/s taking account of the discussion in **3.1**.

Figure 10 shows the dependence of bER on the writing field H_w for various K_u/K_{bulk} values where (a) 4 Tbpsi and the grain number mn = 4 (2×2) and (b) 4 Tbpsi and mn = 9 (3×3 grain arrangement). The minimum K_u/K_{bulk} values for 10 years of archiving are 0.19 and 0.52 for mn = 4 and 9, respectively. As a result, the bER value is more than 10^{-3} under the conditions used in this study for 4 Tbpsi. A serious problem in HAMR is that writing becomes difficult if the damping constant just below the Curie temperature is small.

Then, we examined the writing property for 2 Tbpsi instead of 4 Tbpsi as shown in Fig. 11 for (a) the grain number per bit mn = 8 (4×2 and the mean grain size D_m = 5.4 nm), (b) mn = 12 (4×3 and D_m = 4.2 nm), and (c) mn = 16 (4×4 grain arrangement and D_m = 3.5 nm) considering the discussion in **3.3**. The minimum K_u/K_{bulk} values for 10 years of archiving are 0.19, 0.31, and 0.45 for mn = 8, 12, and 16, respectively.

The difference between the calculation conditions in Fig. 11 (a) and Fig. 10 (a) is simply the grain row number or the recording density, and the D_m values are the same. A bER value of less than 10^{-3} can be achieved for 2 Tbpsi for a statistical reason. The H_w values necessary for bER = 10^{-3} are about 15, 14, and 13 kOe for mn = 8 (K_u/K_{bulk} = 0.4), 12 (0.4), and 16 (0.45), respectively. The writing properties are also almost the same regardless of the grain number under a constant recording density. A high writing field is necessary if the damping constant just below the Curie temperature is small.

4. Conclusions

We can divide the topic of increasing writing field sensitivity into four problems using the bit error rate calculated with our model for heat-assisted magnetic recording, and we discuss the calculation parameters related to the problems.

(1) Write-error problem

Reducing the anisotropy constant ratio K_u/K_{bulk} and/or the linear velocity v is effective in reducing write-error, namely, in increasing the writing field sensitivity.

(2) Erasure-after-write problem

Erasure-after-write must be sufficiently low in a low writing field region. Increasing K_u/K_{bulk}, the thermal gradient for the down-track direction, and/or the grain column number in one bit is effective in reducing erasure-after-write.

(3) Statistics problem

Increasing the grain number per bit under a constant mean grain size is effective in increasing the writing field sensitivity for a statistical reason. However, increasing the grain number under a constant recording density is ineffective. Nevertheless, there is a statistical effect since the recording time window decreases and the attempt period increases.

(4) Damping constant problem

When the Gilbert damping constant α is small, writing is difficult and a high writing field is necessary since the attempt period is long.

As a result of optimization considering the four problems, when α = 0.1, a writing field of about 8 kOe is necessary for 4 Tbpsi and v = 10 m/s. On the other hand, when α = 0.01, a writing field of about 13 kOe is necessary for 2 Tbpsi and v = 5 m/s under the conditions used in this study.

Acknowledgement We acknowledge the support of the Advanced Storage Research Consortium (ASRC), Japan.

References

1) S. H. Charap, P. -L. Lu, and Y. He: *IEEE Trans. Magn.*, **33**, 978 (1997).
2) T. Kobayashi, F. Inukai, K. Enomoto, and Y. Fujiwara: *J. Magn. Soc. Jpn.*, **41**, 1 (2017).
3) T. Kobayashi, Y. Nakatani, F. Inukai, K. Enomoto, and Y. Fujiwara: *J. Magn. Soc. Jpn.*, **41**, 52 (2017).
4) T. Kobayashi, Y. Nakatani, K. Enomoto, and Y. Fujiwara: *J. Magn. Soc. Jpn.*, **42**, 15 (2018).
5) T. Kobayashi, Y. Nakatani, and Y. Fujiwara: submitted to *J. Magn. Soc. Jpn.*.
6) J. -G. Zhu and H. Li: *IEEE. Trans. Magn.*, **49**, 765 (2013).
7) T. Kobayashi, Y. Isowaki, and Y. Fujiwara: *J. Magn. Soc. Jpn.*, **39**, 8 (2015).
8) T. Kobayashi, Y. Isowaki, and Y. Fujiwara: *J. Magn. Soc. Jpn.*, **40**, 28 (2016).
9) J. -U. Thiele, K. R. Coffey, M. F. Toney, J. A. Hedstrom, and A. J. Kellock: *J. Appl. Phys.*, **91**, 6595 (2002).
10) T. Ono, H. Nakata, T. Moriya, N. Kikuchi, S. Okamoto, O. Kitakami, and T. Shimatsu: *Appl. Phys. Express*, **9**, 123002 (2016).
11) T. Kobayashi, T. Kitayama, and Y. Fujiwara: *J. Magn. Soc. Jpn.*, **36**, 282 (2012).
12) Y. Isowaki, T. Kobayashi, and Y. Fujiwara: *J. Magn. Soc. Jpn.*, **38**, 1 (2014).
13) M. Mansuripur, and M. F. Ruane: *IEEE Trans. Magn.*, **MAG-22**, 33 (1986).

Received Apr. 14, 2018; Accepted Jul. 11, 2018

Editorial Committee Members・Paper Committee Members

Notice for Photocopying

編 集 委 員・論 文 委 員

複写をされる方へ

Journal of the Magnetics Society of Japan
Vol. 42 No. 5 (通巻第 299 号) 2018 年 9 月 1 日発行

Vol. 42 No. 5 Published Sep. 1, 2018
by the Magnetics Society of Japan
Tokyo YWCA building Rm207, 1–8–11 Kanda surugadai, Chiyoda-ku, Tokyo 101–0062
Tel. +81–3–5281–0106 Fax. +81–3–5281–0107

Printed by JP Corporation Co., Ltd.
2–3–36, Minamikase, Saiwai-ku, Kanagawa 212–0055
Advertising agency: Kagaku Gijutsu-sha

発行：（公社）日本磁気学会 101–0062 東京都千代田区神田駿河台 1–8–11 東京YWCA会館 207 号室
製作：ジェイピーコーポレーション 212–0055 神奈川県川崎市幸区南加瀬 2–3–36 Tel.（044）571–5815
広告取扱い：科学技術社 111–0052 東京都台東区柳橋 2–10–8 武田ビル 4F Tel.（03）5809–1132